Instability waves in a low-Reynolds-number planar jet investigated with hybrid simulation combining particle tracking velocimetry and direct numerical simulation

TAKAO SUZUKI[1]†, HUI JI[2]‡ AND FUJIO YAMAMOTO[2]

[1]Acoustics and Fluid Mechanics, The Boeing Company, Seattle, WA 98124-2207, USA

[2]Graduate School of Engineering, University of Fukui, 3-9-1 Bunkyo, Fukui 910-8507, Japan

Instability waves in a laminar planar jet are extracted using hybrid unsteady-flow simulation combining particle tracking velocimetry (PTV) and direct numerical simulation (DNS). Unsteady velocity fields on a laser sheet in a water tunnel are measured with time-resolved PTV; subsequently, PTV velocity fields are rectified in a least squares sense so that the equation of continuity is satisfied, and they are transplanted to a two-dimensional incompressible Navier–Stokes solver by setting a multiple of the computational time step equal to the frame rate of the PTV system. As a result, the unsteady hybrid velocity field approaches that of the measured one over time, and we can simultaneously acquire the unsteady pressure field. The resultant set of flow quantities satisfies the governing equations, and their resolution is comparable to that of numerical simulation with the noise level much lower than the original PTV data. From hybrid unsteady velocity fields, we extract eigenfunctions using bi-orthogonal decomposition as a spatial problem for viscous instability. We also investigate stability/convergence characteristics of the hybrid simulation referring to linear stability analysis.

1. Introduction

Instability waves, particularly their linear behaviours, in a jet have been analysed in many studies. For example, symmetric and asymmetric instability modes in a planar jet were investigated by Sato (1960), where velocity fluctuations and mean-velocity fields were measured at low Reynolds numbers to demonstrate the inviscid linear theory (i.e. based on the Rayleigh equation). Later, a compressible planar jet was theoretically studied using an analytic velocity profile by Blumen (1971), while for viscous instabilities, the Orr–Sommerfeld equation was solved by Maslowe (1991) for the Bickley jet (most of these analytic approaches were summarized by Drazin & Reid 1981). Furthermore, details of the Reynolds-number dependence were numerically studied by Morris (1976) for a round jet, and the nonlinear characteristics in a mixing layer were analysed by Huerre (1980). These organized disturbances, evolving into large-scale vortices, were visualized in a laminar round jet by Mollendorf &

† Email address for correspondence: takao@its.caltech.edu
‡ Present address: Powertrain Development Division, Mazda Motor Corporation, Hiroshima 730-8670, Japan

Gebhart (1973). Similarly, large-scale vortical structures in a turbulent mixing layer were observed by Brown & Roshko (1974).

Although it is almost certain that eigenfunctions from linear stability analysis capture dynamics of small disturbances in a jet, extracting or quantifying instability waves is non-trivial in experiments. For example, Arndt, Long & Glauser (1997) performed proper orthogonal decomposition (POD) with multi-point pressure measurement and showed that large-scale structures grow, saturate and decay in the streamwise direction, which are qualitatively consistent with linear stability analysis. Citriniti & George (2000) similarly conducted multi-point velocity measurement to exhibit cross-sectional POD modes. These studies, however, have neither compared the experimental results with eigenfunctions nor quantified their amplitude. For excited jets, several studies have directly compared pressure or velocity fluctuations with eigenfunctions in planar jets (Sato 1960) or round jets (Zaman & Hussain 1980; Mankbadi 1985; Tam & Morris 1985) and reported good agreement. In unforced jets, Suzuki & Colonius (2006) identified the instability-wave amplitude based on a least squares approach using phased-array pressure data in the near field. Most of these studies, however, have compared statistical data, in which instantaneous flow fields are unrecoverable and instantaneous phase information is missing. Moreover, all these studies have processed pointwise measurement data. Difficulty of post-processing experimental data lies in the low spatial resolution and the high noise level, which prohibit quantitative analysis using differentiated flow quantities.

On the other hand, several research groups have explored techniques that reconstruct complete flow fields from sparse dataset in applications other than jet flows. Karniadakis pioneered this field and proposed a technique that recovers velocity fields from image measurement, such as particle image velocimetry (PIV), using POD (Ma *et al.* 2003; Sirisup *et al.* 2004). While POD approaches combined with the Galerkin projection are convenient to reconstruct representative motion, they require a large set of modes to recover detailed non-stationary motion. Another candidate may be the estimator for state-space control proposed by Bewley & Liu (1998), yet the theories primarily represent dynamics of a linear system. Other researchers have focused on integration of experimental data and computational fluid dynamics (CFD). Nisugi, Hayase & Shirai (2004) and Yamagata, Hayase & Higuchi (2008) introduced an unsteady-flow simulation technique incorporating with time-resolved experimental data as a feedback system. Recently, our group developed a hybrid unsteady-flow simulation technique combining particle tracking velocimetry (PTV) and direct numerical simulation (DNS). This approach is able to reconstruct unsteady flow fields from noisy image measurement and to clearly capture non-periodic vortical structures at low Reynolds numbers (Suzuki, Ji & Yamamoto 2009*a*; Suzuki *et al.* 2009*b*).

The basic procedures of the hybrid simulation are as follows. To acquire unsteady velocity fields from experiments, we conduct time-resolved PIV/PTV. In Suzuki *et al.* (2009*a*, *b*), we measured unsteady flows past an airfoil on a laser sheet in a water tunnel. By synchronizing the computational time step with the frame rate of the measurement system, we feed the PIV/PTV velocity field into that of the two-dimensional DNS. Here, the hybrid velocity field is given by a linear combination between the PIV/PTV velocity field and that marched from a previous time step with the DNS, and the weight between them is determined such that all growing modes of the numerical system are suppressed (see figure 1 for a conceptual diagram). As a result, the deviation of the hybrid velocity field from the experimental one is diminished in the course of time. Thus, we can acquire not only unsteady velocity
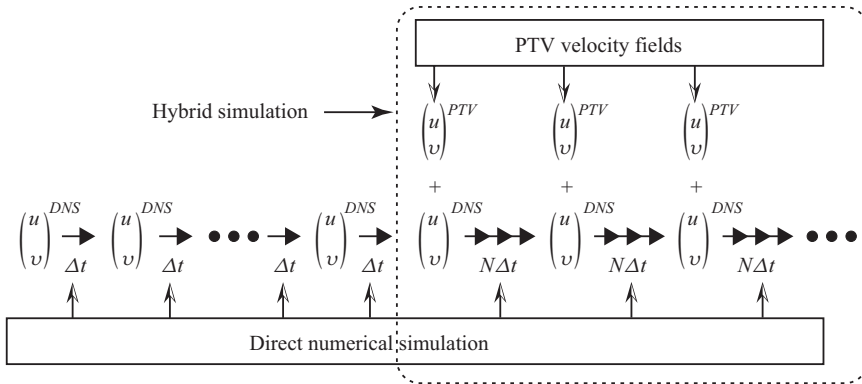
FIGURE 1. Conceptual diagram of the hybrid algorithm combining PTV and DNS.

fields but also pressure fields that are compatible with the governing equations from time-resolved velocity measurement. The resolution of the hybrid velocity field is comparable to that of numerical simulation at low Reynolds numbers so that flow quantities are differentiable for quantitative analysis.

The objective of this research is to investigate the features of the hybrid unsteady-flow simulation based on planar-jet flows referring to linear stability analysis and to extract instability waves from velocity image measurement. We measure unsteady velocity fields of a planar jet in the Reynolds-number range of $Re = 500$–4000 in a water tunnel with time-resolved PTV, similar to our previous airfoil study. Two-dimensional hybrid simulations solving the motion on the laser sheet suppress excessive high-frequency/wavenumber components of the PTV data but retain large-scale vortical structures in the shear layers. The measurement noise level diminishes with decreasing weight on the PTV velocity field relative to that updated with the DNS at each hybrid time step. To identify amplitude of instability waves, we extract eigenfunctions of the Orr–Sommerfeld equation by introducing 'bi-orthogonal decomposition' (see Morse & Feshbach 1953 for the mathematical frame work), or sometimes referred to as 'normal-mode decomposition' (Ahluwalia & Keller 1977). Since Salwen & Grosch (1981) introduced this approach for a viscous boundary layer, several studies have applied it, for example, to an incompressible boundary layer (Hill 1995; Tumin 2003), the Poiseuille flow (Tumin 1996), a compressible boundary layer (Suzuki & Lele 2003a; Tumin 2007), and a compressible mixing layer (Suzuki & Lele 2003b; Barone & Lele 2005). These studies have demonstrated the applicability of bi-orthogonal decomposition to theoretical or computational flows (Hill 1995 and Tumin 2003 have extensive lists of these studies); however, applying it to experimental data is more challenging because it requires high-order derivatives, which readily amplify measurement noise in practice.

Furthermore, we evaluate the necessary weight on the PTV velocity field in the hybrid algorithm by analysing the growth rates of the Kelvin–Helmholtz instability as well as the amplification rate of the entire numerical system. The results indicate that the hybrid velocity field approaches the measured one if the weight on the PTV data overcomes the maximum amplification rate of modes spatially developing when the hybrid simulation starts with the initial DNS flow field. We also discuss the Reynolds-number dependence as well as the effects of unresolvable-scale motions and three-dimensional dynamics.
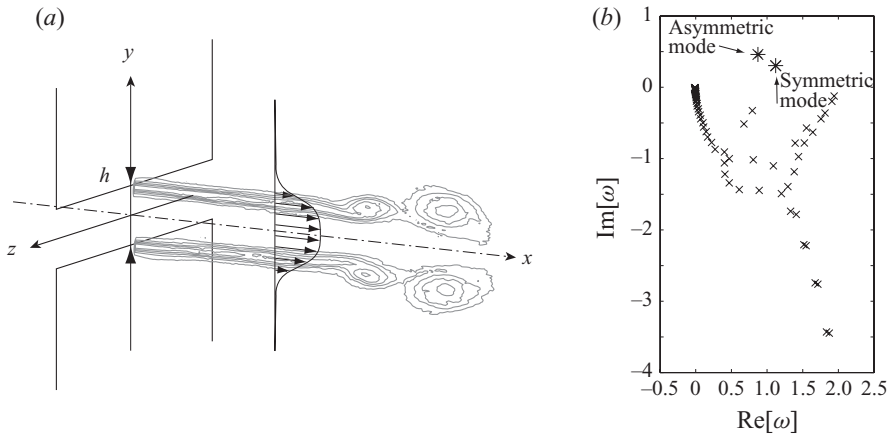
FIGURE 2. (*a*) Coordinate system of the planar jet. (*b*) Example of eigenvalue distribution for a temporal problem. Complex ω solved with the spectral method is mapped for $\alpha = 2$ at $Re = 1000$. Two unstable modes are denoted with *.

The rest of the paper is organized as follows. After the introduction, basic characteristics of instability waves in a planar jet are reviewed and bi-orthogonal decomposition is introduced based on linear stability analysis in §2. Next, experimental set-ups and flow conditions are described in §3; subsequently, numerical approaches including the algorithm and procedures of the hybrid simulation are summarized in §4. In §5, notable features of the hybrid simulation including noise suppression and the weight between the PTV and DNS velocity fields are discussed over a range of Reynolds numbers, and the hybrid flow field is compared with a previous experiment by Sato (1960). To demonstrate the capability of the hybrid simulation, instability waves in the hybrid velocity fields are analysed using bi-orthogonal decomposition in §6, followed by the conclusion in §7, in which important findings and implications are summarized.

2. Instability waves and linear stability analysis

2.1. *Orr–Sommerfeld equation*

In this study, we analyse the viscous instability of an incompressible planar jet based on the Orr–Sommerfeld equation. Assuming that the mean-velocity field is transversely sheared and unsteady disturbances can be linearly expressed as $\sim\exp\left[-\mathrm{i}\left(\omega t - \alpha x\right)\right]$, where ω denotes the angular frequency and α the wavenumber in the streamwise direction (see figure 2*a* for the coordinate system), the incompressible Navier–Stokes equations in two dimensions can be simplified as the Orr–Sommerfeld equation:

$$\mathscr{L}\psi(y) \equiv \frac{1}{Re}\left(\frac{\mathrm{d}^2}{\mathrm{d}y^2} - \alpha^2\right)^2 \psi(y) + \mathrm{i}\left(\omega - \alpha U(y)\right)\left(\frac{\mathrm{d}^2}{\mathrm{d}y^2} - \alpha^2\right)\psi(y) + \mathrm{i}\alpha U''(y)\psi(y) = 0,$$

(2.1)

where $\psi(y)$ denotes the transverse part of the stream function (namely $\mathrm{Re}\left[\psi(y)\exp\left(\mathrm{i}\alpha x\right)\right]$ comprises the complete stream function), $\mathscr{L}$ the Orr–Sommerfeld operator and $U(y)$ the streamwise mean-velocity profile. In the following stability analysis, we impose the homogeneous boundary conditions,

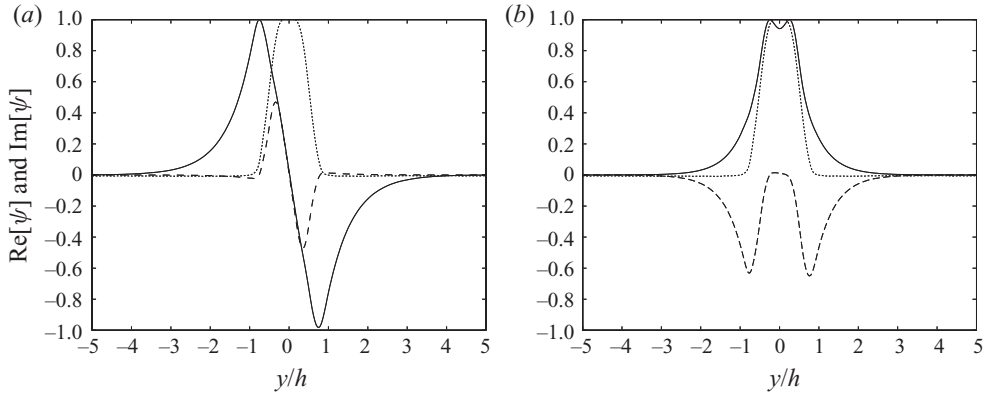$$\psi(y \to \pm\infty) = \psi'(y \to \pm\infty) \equiv 0,$$

(2.2)

FIGURE 3. Temporal eigenfunctions, $\psi(y)$, at $St = 0.15$ with a PTV mean-velocity profile at $x/h = 5$. (*a*) Symmetric mode. (*b*) Asymmetric mode. The real part, whose peak is normalized to unity, is drawn by a solid line, and the imaginary part by a dashed one. The mean streamwise velocity, $U(y)$, is shown by a dotted line for reference.

assuming that the distances to the upper and lower walls of the tunnel are far enough for simplicity (see figure 6 later for the geometry in the experiment).

As an example, the solutions for ω at $Re = 1000$ are plotted in figure 2(*b*). A temporal problem is solved using a spectral method described in § 2.3. In this study, $U(y)$ is given by the time-averaged PTV velocity field, unless otherwise noted. Although the spatial problem is more relevant to the current geometry, we analyse the temporal growth rate in this section to estimate the weight between the PTV and DNS velocity fields later for the hybrid algorithm. We discuss spatial instabilities in §§ 2.2 and 6 for bi-orthogonal decomposition, yet many of their trends are common to those for temporal instabilities.

For an incompressible planar jet with a typical top-hat velocity profile, there are two unstable modes. The asymmetric mode generally has a higher growth rate than that of the symmetric mode (refer to Sato 1960; Blumen 1971). Figure 3 depicts the eigenfunctions, $\psi(y)$, near the most unstable frequency ($St = 0.15$, where $St \equiv fh/u_{jet}$, f being the frequency, h the nozzle exit height and u_{jet} the jet velocity defined later). Here, we refer the symmetry based on the streamwise velocity or pressure; hence, the shapes of $\psi(y)$ appear conversely.

Figure 4(*a*) shows the growth rates as a function of the Strouhal number at $Re = 1000$. These modes peak near $St \approx 0.15$ and decay beyond the neutral stable frequency (i.e. the cross-over points at $St \gtrsim 0.3$). Figure 4(*b*) plots the maximum growth rates at several downstream stations. Both growth rates decrease as the velocity profile spreads downstream; consequently, instability waves eventually saturate and decay somewhere $x/h > 10$. The eigenfunction profiles, $\psi(y)$, accordingly become gentler downstream with decreasing peak Strouhal number. We should remember that the growth rates in figure 4 are plotted assuming a parallel flow at each x; hence, they are considered to be 'local' growth rates. In contrast, growth rates amplifying the entire system with a given two-dimensional mean-velocity field are referred to 'global' growth rates, which cannot be obtained from this simple analysis (refer to Huerre & Monkewitz 1990 and Theofilis 2003 for explanations about the local versus global instability modes).
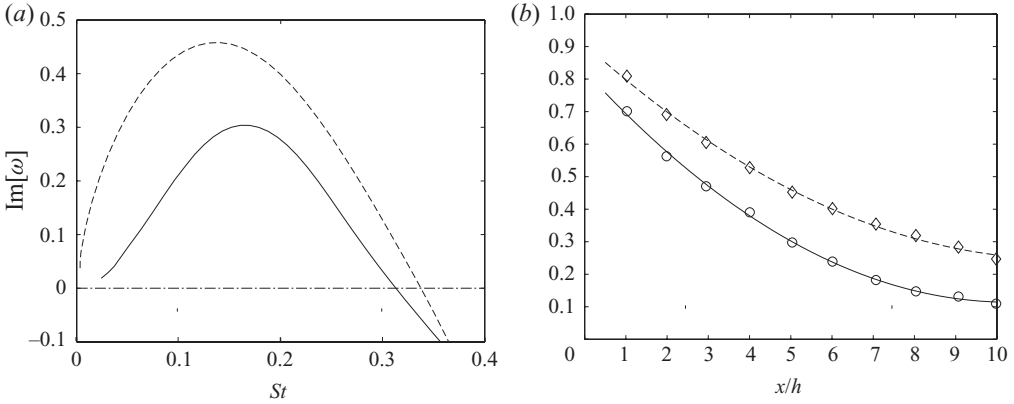
FIGURE 4. Temporal growth rates of instability waves solved based on the Orr–Sommerfeld equation at $Re = 1000$. (a) Growth rates at $x/h = 5$. Line patterns: ——, symmetric mode; — — —, asymmetric mode. (b) Maximum growth rates at various stations. Symbols: ○, symmetric mode; ◇, asymmetric mode. Line patterns are the same as (a) and fitted with quadratic curves.
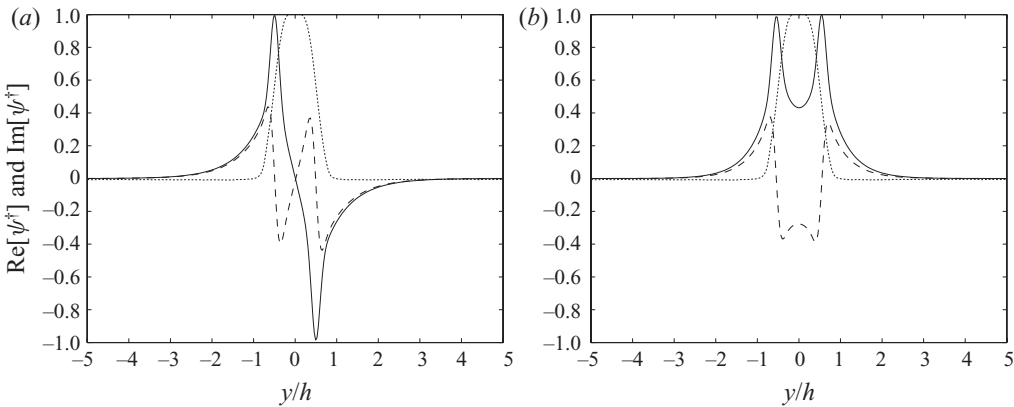

FIGURE 5. Adjoint eigenfunctions, $\psi^\dagger(y)$, corresponding to figure 3 at $St = 0.15$. (a) Symmetric mode. (b) Asymmetric mode. Line patterns are the same as figure 3.

2.2. *Adjoint equation and bi-orthogonal decomposition*

Because the Orr–Sommerfeld equation is not self-adjoint, its adjoint equation must be introduced to determine the amplitude of instability waves using bi-orthogonal decomposition. Integrating (2.1) by parts with (2.2), the adjoint equation can be derived as

$$\mathscr{L}^\dagger \psi^\dagger(y) \equiv \frac{1}{Re}\left(\frac{\mathrm{d}^2}{\mathrm{d}y^2} - \alpha^2\right)^2 \psi^\dagger(y) + \mathrm{i}(\omega - \alpha U(y))\left(\frac{\mathrm{d}^2}{\mathrm{d}y^2} - \alpha^2\right)\psi^\dagger(y)$$
$$- \mathrm{i}2\alpha U'(y)\psi^\dagger(y) = 0, \quad (2.3)$$

where $\mathscr{L}^\dagger$ denotes the adjoint Orr–Sommerfeld operator, and the disturbances are assumed to take the adjoint linear form; i.e. $\sim\exp\left[\mathrm{i}(\omega t - \alpha x)\right]$. This equation has the same discrete solutions for ω and α as (2.1). Figure 5 draws the shapes of $\psi^\dagger(y)$ corresponding to figure 3. They depict sharper peaks near the inflection points in the shear layers compared with the original eigenfunctions.

Using (2.1) and (2.3) and assuming that the eigenfunctions as well as the mean velocity vanish as $y \to \pm\infty$, the following relation was derived by Salwen & Grosch (1981):

$$\int_{-\infty}^{\infty} \Psi^{\dagger} \mathscr{L} \Psi + \Psi \mathscr{L}^{\dagger} \Psi^{\dagger} \mathrm{d}y = \frac{\partial}{\partial t} J_t + \frac{\partial}{\partial x} J_x, \tag{2.4}$$

where

$$J_t\left(\Psi^{\dagger}, \Psi\right) \equiv \int_{-\infty}^{\infty} \left[\frac{\partial \Psi^{\dagger}}{\partial y}\frac{\partial \Psi}{\partial y} + \frac{\partial \Psi^{\dagger}}{\partial x}\frac{\partial \Psi}{\partial x}\right] \mathrm{d}y, \tag{2.5a}$$

$$\begin{aligned}
J_x\left(\Psi^{\dagger}, \Psi\right) \equiv \frac{1}{Re} \int_{-\infty}^{\infty} &\left[\Psi^{\dagger}\frac{\partial^3 \Psi}{\partial x^3} - \frac{\partial \Psi^{\dagger}}{\partial x}\frac{\partial^2 \Psi}{\partial x^2} + \frac{\partial^2 \Psi^{\dagger}}{\partial x^2}\frac{\partial \Psi}{\partial x} - \frac{\partial^3 \Psi^{\dagger}}{\partial x^3}\Psi \right. \\
&\left. + 2\frac{\partial^2 \Psi^{\dagger}}{\partial x \partial y}\frac{\partial \Psi}{\partial y} - 2\frac{\partial \Psi^{\dagger}}{\partial y}\frac{\partial^2 \Psi}{\partial x \partial y}\right] \mathrm{d}y - \int_{-\infty}^{\infty} \left[\Psi^{\dagger}\frac{\partial^2 \Psi}{\partial t \partial x} + \frac{\partial^2 \Psi^{\dagger}}{\partial t \partial x}\Psi\right] \mathrm{d}y \\
&+ \int_{-\infty}^{\infty} \left[U\left(2\frac{\partial \Psi^{\dagger}}{\partial y}\frac{\partial \Psi}{\partial y} + \frac{\partial^2 \Psi^{\dagger}}{\partial y^2}\Psi - \Psi^{\dagger}\frac{\partial^2 \Psi}{\partial x^2} + \frac{\partial \Psi^{\dagger}}{\partial x}\frac{\partial \Psi}{\partial x} - \frac{\partial^2 \Psi^{\dagger}}{\partial x^2}\Psi\right)\right] \mathrm{d}y,
\end{aligned} \tag{2.5b}$$

and each discrete solution, referred to as an 'eigenmode' here, is expressed as $\Psi_m(t, x, y) \equiv \psi(y) \exp\left[-\mathrm{i}\left(\omega t - \alpha_m x\right)\right]$ and its adjoint solution as $\Psi_n^{\dagger}(t, x, y) \equiv \psi^{\dagger}(y) \exp\left[\mathrm{i}\left(\omega t - \alpha_n x\right)\right]$ (the wavenumbers are labelled with the subscripts m and n for a spatial problem discussed below); hence, the system is expressed using the original derivatives as opposed to a periodic form with ω and α, as shown in (2.1) and (2.3).

Because the eigenmodes for instability waves take discrete solutions, the integral, (2.5a,b), acts as an inner product for a temporal and spatial problem, respectively, in the bi-orthogonal system. In a spatial problem, i.e. with given ω, $\partial J_t/\partial t$ vanishes, while the partial derivative of x acting on J_x yields $\mathrm{i}(\alpha_m - \alpha_n)$, which vanishes only if two wavenumbers are identical. Conversely, J_x vanishes only if $\Psi^{\dagger}$ corresponds to the adjoint solution of Ψ. Therefore, we can determine the complex amplitude of a specific eigenmode (denoted by Ψ_m) from an arbitrary disturbance by substituting $\int \hat{u} \mathrm{d}y$, where $\hat{u}$ being the streamwise velocity in the frequency domain, into Ψ and by calculating

$$a_m = \frac{J_x(\Psi_m^{\dagger}, \Psi)}{J_x(\Psi_m^{\dagger}, \Psi_m)} \tag{2.6}$$

at each axial station. We are also able to calculate the amplitude of a temporal eigenfunction by similarly using J_t.

We apply bi-orthogonal decomposition to hybrid velocity fields in §6. By assuming the flow to be locally parallel, we compute complex amplitudes of both symmetric and asymmetric instability waves as a function of x for a spatial problem. Because this decomposition requires up to the second-order derivatives of the velocity component in (2.5b), i.e. $\partial^3 \psi/\partial x^3$, it is challenging to apply this technique for experimental data, which readily amplify measurement noise by spatial differentiation.

We could circumvent higher derivatives using an alternative approach, such as one analysed by Tumin (2003) and Denissen & White (2009), where they have formulated the viscous instability problem in terms of primitive variables including pressure fluctuation. However, because complete flow quantities are usually unavailable in

experiments, those studies have introduced decomposition based on partial flow information together with regularization, resulting in pre-selection of eigenmodes and optimization of additional parameters. By using hybrid velocity fields, we can avoid such ambiguities associated with mode selection and regularization parameters. Moreover, unsteady pressure fields are actually available in our approach, even if we decompose fluctuations using primitive variables.

2.3. *Spectral method for computation*

To compute complex ω for a temporal problem or complex α for a spatial problem of (2.1)–(2.3) with a given $U(y)$, we use the Galerkin method, which was introduced by Orszag (1971) for the viscous instability analysis. For a temporal problem, we recast the Orr–Sommerfeld equation as

$$\left[\left(\frac{d^2}{dy^2} - \alpha^2\right)^2 - i\alpha Re U\left(\frac{d^2}{dy^2} - \alpha^2\right) + i\alpha Re U''\right]\psi = -\omega \cdot iRe\left(\frac{d^2}{dy^2} - \alpha^2\right)\psi, \quad (2.7)$$

and express the equation above in the matrix form using a set of the orthogonal basis functions for ψ. Namely,

$$\psi(y) \equiv \sum_{n=0}^{N} c_n P_n(y), \quad (2.8)$$

where P_n denotes the nth basis function and c_n its coefficient. We typically choose P_n such that they satisfy the boundary conditions (2.2). Subsequently, we can solve it as an eigenvalue problem, where the eigenvalue ω with the greatest imaginary part signifies the most unstable mode and its eigenvector specifies the coefficients c_n producing the eigenfunction with the orthogonal bases.

On the other hand, the Orr–Sommerfeld equation cannot be recast in a linear form of α for a spatial problem; hence, (2.1) is rewritten in a form analysed by Bridges & Morris (1984) as follows:

$$\left[\left(\frac{d^2}{dy^2} - \alpha^2\right)^2 + i\omega Re \frac{d^2}{dy^2}\right]\psi = \alpha \cdot iRe\left[U\left(\frac{d^2}{dy^2} - \alpha^2\right) - U'' + \alpha\omega\right]\psi. \quad (2.9)$$

Accordingly, the eigenvalue problem with respect to α can be solved iteratively for a given ω. The matrix equation corresponding to (2.9) can be symbolically expressed as

$$A(\omega, \alpha^i)c = \alpha^{i+1} B(\omega, \alpha^i)c, \quad (2.10)$$

where c represents a vector form of the coefficients for the basis functions and the superscript i denotes the iteration counter. Once we find the converged solution at the most upstream station, this becomes the initial guess for the next station. We perform iteration until the difference of the eigenvalue from the previous iteration becomes $\left|\alpha^{i+1} - \alpha^i\right| < 10^{-3}$. The adjoint equation (2.3) is also solvable with the same procedures.

To solve these problems in an infinitely extended domain, we take the approach analysed by Spalart, Moser & Rogers (1991), where the eigenfunctions are expanded using the Jacobi polynomials of $(\alpha, \beta) = (1, 1)$. Their polynomial-series representation can be defined in $-1 \leqslant \eta \leqslant 1$ as

$$P_n^{(1,1)}(\eta) \equiv \sum_{k=0}^{n} \left(\frac{\eta - 1}{2}\right)^k \left(\frac{\eta + 1}{2}\right)^{n-k}. \quad (2.11)$$

The domain of η is mapped into the physical space, $-\infty < y < \infty$, using $\eta \equiv \tanh(y/y_0)$, where $y_0 = 1.0$ is selected in this study. Accordingly, the basis functions vanish as $y \to \pm\infty$. We take the grid for y from that of the hybrid simulation ($N_y = 300$ in $-10 \leqslant y \leqslant 10$ for the baseline case), and use $N = 64$ polynomials to expand eigenfunctions. Appendix A discusses further details of the spectral method and its accuracy.

Although the computational approach above provides local growth rates of instability waves, we wish to estimate the temporal growth rate of the entire flow field, i.e. global instability waves, to deduce the weight between the PTV and DNS velocity fields later for the hybrid algorithm. Moreover, global eigenfunctions representing spatially developed instability waves in two dimensions are useful to compare with the results of bi-orthogonal decomposition in §6. To construct 'surrogate' global eigenfunctions in two dimensions, we connect local eigenfunctions with α in the streamwise direction assuming the spreading rate of the jet to be small. Namely, we treat

$$\Psi_{(2)}(x, y) \equiv \psi(x; y) \exp\left[i \int_0^x \alpha(x') x' \mathrm{d}x'\right] \qquad (2.12)$$

as an approximate global eigenfunction, where $\psi(x; y)$ denotes a sectional eigenfunction solved with a local velocity profile at a streamwise station x. To normalize $\psi(x; y)$, we set $|\psi(x; y)|$ to be unity at each station by following Herbert (1997).

For a spatial problem in two dimensions, α is a complex function of x, and $\Psi_{(2)}(x, y)$ is calculated for a given frequency. To solve a temporal problem, (2.12) is similarly integrated with a constant real α, but imposing several additional assumptions. These assumptions are justified in Appendix B together with the estimation of temporal growth rates using surrogate eigenfunctions. To rigorously compute temporal eigenfunctions in two dimensions, an approach developed by Theofilis (2000), for example, can be adopted.

3. Experimental apparatuses and flow conditions

To create a planar-jet flow, we fabricated a two-dimensional nozzle of a $w = 79$ mm span-width with a 10 mm thick panel on both sides and of an $h = 5$ mm exit height, which is taken as the length scale; hence, the aspect ratio yields about 16. Refer to figure 6 for the nozzle geometry as well as the experimental set-up. The half-angle of the nozzle contraction is 15°, and no tripping device was used so that the jet flow was expected to be initially laminar at the exit. The nozzle was installed in a 100 mm × 100 mm cross-section of a water tunnel; thereby, the nozzle height being 1/20 of the tunnel height, and the distance from the exit to the end of the test section was 1160 mm. The contact surfaces between the tunnel wall and the nozzle were sealed with rubber sheets of 0.5 mm thickness. Both nozzle and water tunnel are made of transparent acrylic resin for optical access. Water that is once accumulated in a tank first enters a honeycomb section, passes through the test section of the tunnel, and recirculates via a water pump.

A 4 W continuous argon-ion laser (wavelength of 488 nm, Spectra-Physics 2017-04SF) was used for a light source. A laser beam was spread using a half-cylindrical lens to create a laser sheet inserted from the bottom. The laser-sheet plane was aligned approximately at the mid-span of the test section (40 mm from the sidewall) in the streamwise direction. To capture flow images, a CMOS high-speed video camera
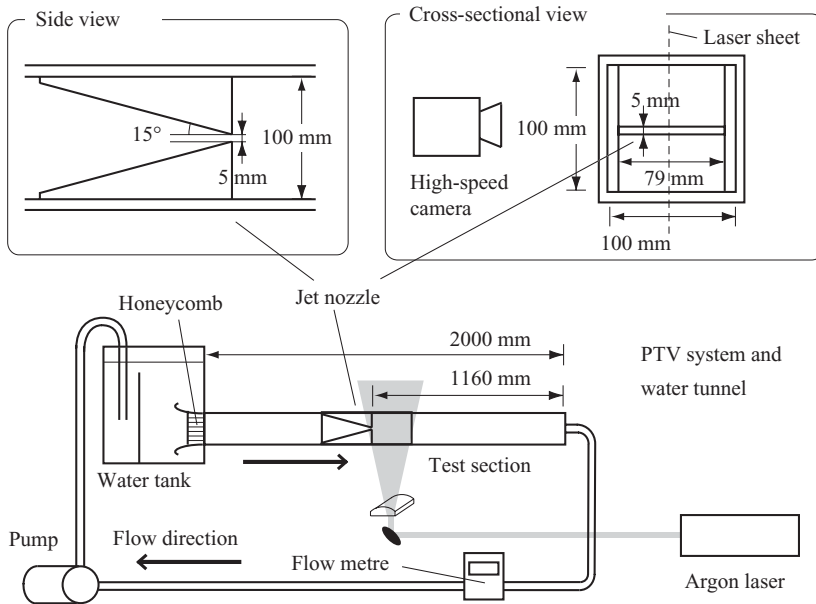
FIGURE 6. Experimental apparatuses including the planar-jet nozzle and the water tunnel as well as the PTV system.

(Photoron, FASTCAM-MAX) was focused on this sheet from the spanwise direction. The focus was confirmed by installing a scaling plate at the mid-span of the test section before running tests. Approximately a 50 mm × 50 mm square region of the test section immediately downstream of the nozzle exit was recorded by the camera with the resolution of 1024 × 1024 pixels, except for the $Re = 4000$ case, where the domain was halved in the transverse direction due to a higher frame rate, and the resolution was accordingly changed to 1024 × 512 pixels. For each flow condition, more than 6000 frames were taken by setting the shutter speed to be equal to the frame rate of the camera, but only sampling periods after the flow reaches a quasi-stationary state are processed as explained later.

We seeded silicon dioxide tracer particles (MATSUMOTO Microsphere, F-793D) of approximately 30 μm in the diameter into water and tuned their density so that more than 10 000 particles can be identified at each frame. Particle velocity is determined by tracking individual particles through four consecutive frames (Nishino, Kasagi & Hirata 1989). At each frame, at least 7000 particles can be traced in 1024 × 1024 pixels (and approximately half only for the $Re = 4000$ case because of the halved domain mentioned above). A typical instantaneous flow field consisting of particle velocities is shown in figure 7.

To assign the velocity components at the computational grids, six neighbouring PTV velocity vectors are selected for each grid point, and the first-order interpolation is applied to determine the velocity components based on the least squares method. The results of the hybrid simulation are insensitive to the number of sampled neighbouring particles and the order of the interpolation. Uncertainties associated with the velocity rearrangement schemes were extensively evaluated in Suzuki *et al.* (2009*a*).

In this study, we tested four different Reynolds numbers from $Re = 500$ to 4000, defining it based on the nozzle height; namely $Re \equiv u_{jet} h / \nu$, where $u_{jet} \equiv \int \overline{u}(y) \mathrm{d}y / h$ and ν is the kinematic viscosity. Table 1 summarizes these flow conditions as well as

Case	Re	u_{jet} (mm s^{-1})	T_{water}	Frame rate	Δt^{DNS}	Δt^{PTV}	N
A	500 (500)	96	22 °C	500 f.p.s.	7.68×10^{-3}	3.84×10^{-2}	5
B	1000 (930)	164	29 °C	1000 f.p.s.	6.06×10^{-3}	3.27×10^{-2}	5
C	2000 (2000)	384	22 °C	2000 f.p.s.	$4.80/7.68 \times 10^{-3}$	3.84×10^{-2}	8/5
D	4000 (4000)	823	16 °C	4000 f.p.s.	5.28×10^{-3}	4.23×10^{-2}	8

TABLE 1. Experimental conditions. u_{jet} denotes the jet velocity based on the flow rate, T_{water} the water temperature and $N \equiv \Delta t^{PTV}/\Delta t^{DNS}$, where $\Delta t^{PTV} \equiv u_{jet}/(\text{frame rate} \times h)$. Parentheses in the second column indicate the Reynolds numbers actually measured from PTV. Dual values for $Re = 2000$ correspond to different grids for the resolution study.
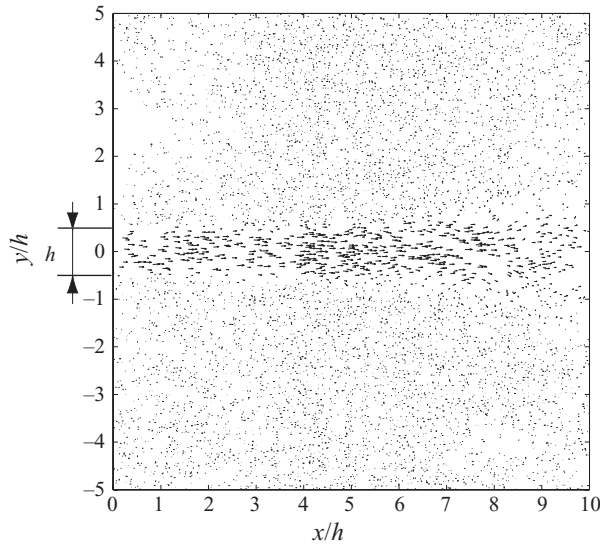

FIGURE 7. Example of a particle-velocity field acquired with PTV ($Re = 1000$, 8068 particles).

the parameters for the measurement system. By monitoring a flowmeter, we tuned the jet velocity to the designed value via a pump and confirmed its measured velocity with the PTV later. The target Reynolds numbers are listed in table 1 on the left together with the measured ones in the parentheses. The hybrid simulations are performed actually at the measured Reynolds numbers.

Although the nozzle was carefully installed and sealed in the tunnel, a jet flow tended to be attached to either upper or lower wall over a long operating period. Hence, the images were recorded after several vortices were observed from an impulsive start but before the jet began to bend. We then process the data only during the period while the jet flow was quasi-stationary and straight.

4. Hybrid unsteady-flow simulation

The basic procedures of the hybrid simulation are the same as those developed in our previous study. Details of the algorithm and the validation against experiments have been discussed in Suzuki *et al.* (2009*a*) and Suzuki *et al.* (2009*b*), respectively. In the following, the algorithm is summarized in §4.1, followed by the backbone flow solver, i.e. DNS, including numerical treatments specific to planar-jet flows in §4.2.

4.1. *Algorithm of hybrid simulation*

In this study, we process PTV velocity fields, yet general PIV velocity fields are equally applicable to the hybrid algorithm. While PTV may provide higher resolution than PIV under certain conditions, it specifies velocity vectors only at points where tracer particles are identified. Therefore, the velocity components must be reassigned at the designated node points of the simulation.

We represent such velocity components interpolated from PTV data as (U, V) in two dimensions. To feed them to the hybrid simulation, we must rectify them so that they satisfy the governing equations. For incompressible flows, arbitrary velocity fields can satisfy the momentum equation with the time-derivative term so long as no constraint is imposed on the pressure field. Hence, the equation of continuity is the only constraint for the rearranged velocity field. By expressing the rearranged components as (u, v), we define the following least squares cost function:

$$J(u, v, \lambda) \equiv \iint_{\mathscr{D}} (u - U)^2 + (v - V)^2 + \lambda \left(\frac{\partial u}{\partial x} + \frac{\partial v}{\partial y} \right) \mathrm{d}x\mathrm{d}y, \qquad (4.1)$$

where λ is a Lagrangian multiplier, which is a function of space, and $\mathscr{D}$ denotes the domain where the PTV velocity field is available. We recast the velocity field so that the cost function above is minimized. By setting $\partial J/\partial u = 0$, $\partial J/\partial v = 0$ and $\partial J/\partial \lambda = 0$, the rearranged velocity components can be calculated as follows:

$$u = U + \frac{1}{2} \frac{\partial \lambda}{\partial x}, \qquad (4.2a)$$

$$v = V + \frac{1}{2} \frac{\partial \lambda}{\partial y}, \qquad (4.2b)$$

where λ is given by

$$\frac{\partial^2 \lambda}{\partial x^2} + \frac{\partial^2 \lambda}{\partial y^2} = -2 \left(\frac{\partial U}{\partial x} + \frac{\partial V}{\partial y} \right). \qquad (4.3)$$

Here, λ is assumed to be compact in $\mathscr{D}$ when (4.1) is integrated by parts. In reality, because the domain in which the PTV velocity data are available is limited in space, a so-called 'patch function' is introduced, as explained in the next section. The complete analysis including the patch function was performed in Suzuki *et al.* (2009*a*). Thus, the rearranged velocity field is calculated by solving the Poisson equation whose source term is given by the divergence of the PTV velocity field.

Since PTV velocity fields projected only on a laser sheet are available, they are forced to follow the equation of continuity in two dimensions. When three-dimensional and three-component velocity fields were to be acquired, the ambiguity associated with the projection can be removed. An implicit assumption here is that the noise level of the measurement is much higher than the spanwise velocity component. In addition, it should be remembered that the resolvable length scale in the DNS is generally smaller than that of the PTV. The effects of the spanwise motion and the resolution issues are discussed in §§ 5.2 and 5.3. It is also be noted that the correction term of the vector field is solenoidal; hence, the vorticity field, which will be observed throughout the paper, is unchanged by this rearrangement.

To supply the rearranged PTV velocity field into DNS, we start with the original DNS and run it until initial vortices leave the domain in which PTV data are available. Subsequently, we start feeding the PTV velocity field to that marched with the DNS at every N time steps, where N being an integer, by synchronizing N times

the computational time step, Δt^{DNS}, with the frame rate of the PTV system, Δt^{PTV}, as illustrated in figure 1. To readily retain the divergence-free condition mentioned above, we set the hybrid velocity field as the following linear combination:

$$\begin{pmatrix} u \\ v \end{pmatrix}^{Hybrid} = (1 - \epsilon) \begin{pmatrix} u \\ v \end{pmatrix}^{DNS} + \epsilon \begin{pmatrix} u \\ v \end{pmatrix}^{PTV}, \tag{4.4}$$

where the superscript '*DNS*' denotes the velocity components updated with the DNS and '*PTV*' the rearranged PTV velocity components mentioned above. Here, the weight function, ϵ ($0 \leqslant \epsilon \leqslant 1$), is assumed to be a constant in time for the analysis below, but will be multiplied by a function of space (i.e. a patch function) later. The weight can also be optimized in time, and such a technique was introduced in Suzuki *et al.* (2009*b*).

To analyse the convergence of the hybrid algorithm, we define the velocity vector and its error vector of the hybrid simulation as

$$\tilde{\boldsymbol{u}}_n \equiv \begin{pmatrix} \tilde{u} \\ \tilde{v} \end{pmatrix}_n \qquad \text{and} \qquad \boldsymbol{e}_n \equiv \begin{pmatrix} \delta u \\ \delta v \end{pmatrix}_n, \tag{4.5}$$

respectively, where the subscript 'n' denotes the computational time-step counter. Here, the tilde on the top represents the exact quantity, which PTV attempts to measure, as opposed to that including the error in (4.4), and δ denotes the error component of the specified quantity. Hence, we can recover the velocity vector in (4.4) by $\boldsymbol{u}_n \equiv \tilde{\boldsymbol{u}}_n + \boldsymbol{e}_n$ and assume $|\boldsymbol{e}_n| \ll |\boldsymbol{u}_n|$ in the following discussion.

Subsequently, we expand the operator of the DNS solver in a linear fashion and denote the noise component associated with the PTV measurement as $\boldsymbol{w}$. By substituting (4.4) and (4.5) into the DNS operator, we can derive the following recursive relation for $\boldsymbol{e}_n$:

$$\boldsymbol{e}_{n+1} \approx [(1 - \epsilon) \cdot \exp(-\mathrm{i}\omega \Delta t^{PTV})]\boldsymbol{e}_n + \epsilon \boldsymbol{w}_{n+1}, \tag{4.6}$$

where the time step is denoted by Δt^{PTV} and the temporal part of the error term is expressed as $\sim \exp(-\mathrm{i}\omega t)$, ω being complex. Accordingly, assuming that $\boldsymbol{w}$ is independent and identical with the mean zero at each time step, the expected magnitude of the error vector can be estimated as

$$E[|\boldsymbol{e}_{n+1}|^2] \leqslant \left[|\hat{r}|^{2n} + \epsilon^2 \frac{|\hat{r}|^{2n} - 1}{|\hat{r}|^2 - 1} \right] E[|\boldsymbol{w}|^2], \tag{4.7}$$

where $|\hat{r}| \equiv (1 - \epsilon) \cdot \exp(\mathrm{Im}[\omega]\Delta t^{PTV})$. An analogous recursive relation was derived by Suzuki & Colonius (2003).

In principle, we select the time-marching scheme and the spatial differentiation such that their combination is numerically stable for any wavenumbers in the computation. Therefore, the original Navier–Stokes solver should satisfy $\exp(\mathrm{Im}[\omega]\Delta t^{DNS}) \leqslant 1$ in a uniform flow. However, when the given flow field physically excites linear instabilities, the amplification rate, $\exp(\mathrm{Im}[\omega]\Delta t^{PTV})$, can exceed unity during a finite period (it is noted here that the term 'amplification rate' is used for any modes in the entire system including physical and numerical ones, while the 'growth rate' is limited to physical instability throughout this paper). Thus, it is necessary to determine ϵ such that $|\hat{r}| < 1$ is satisfied and the noise component is suppressed in the course of time; namely, the hybrid velocity field is converged to the velocity field attempted to be measured with the PTV. At the same time, it is ensured that the simulated flow field is governed by the PTV measurement, not by the DNS.

Suppose we are able to estimate the maximum global amplification rates including both computational and physical ones. We then wish to choose the weight on PTV as

$$\epsilon > \text{Im} \, [\omega]_{max} \, \Delta t^{PTV}, \tag{4.8}$$

so that the condition $|\hat{r}| < 1$ is guaranteed for small Δt. It is indicated from (4.8) that the contribution from the PTV data, which is only of the order of $O \left(\text{Im} \, [\omega]_{max} \, N \Delta t^{DNS} \right)$, can still be reduced at each hybrid time step if the time step is decreased. This helps suppress noise components and generate smooth velocity fields so that flow quantities become differentiable. Namely, viscous dissipation overcomes the noise level of random errors over time. We discuss the relation between the weight on the PTV data and the growth rate of linear instability waves as well as the amplification rate of the numerical system based on the actual simulation in §5.2.

4.2. *Navier–Stokes flow solver and the patch function*

To march the hybrid velocity field, we solve the incompressible Navier–Stokes equations in two dimensions with staggered grids using the fractional step method (Kim & Moin 1985). The time-marching schemes consist of the third-order Adams–Bashforth scheme for the convection terms and the Crank–Nicholson scheme for the diffusion terms, as shown below:

$$\frac{\hat{u} - u_n}{\Delta t} = -\frac{23 \nabla \cdot (uu)_n - 16 \nabla \cdot (uu)_{n-1} + 5 \nabla \cdot (uu)_{n-2}}{12} + \frac{1}{Re} \Delta \left(\frac{\hat{u} + u_n}{2} \right), \tag{4.9}$$

$$\frac{u_{n+1} - \hat{u}}{\Delta t} = -\nabla \phi_{n+1} - \sigma_0(x) (u_{n+1} - u_c), \tag{4.10}$$

where the subscript n denotes the time-step counter, the second term on the right-hand side of (4.10) is the 'sponge buffer' term explained later and ϕ is given by the following Poisson equation:

$$\Delta \phi_{n+1} = \frac{1}{\Delta t} \nabla \cdot \hat{u} \, . \tag{4.11}$$

For spatial derivatives, we use a four-stencil central-differencing scheme proposed by Kampanis & Ekaterinaris (2006) with lower-order schemes for the boundary points.

To efficiently solve jet flows, rectangular grids are clustered near the nozzle exit and stretched by constant rates in both x and y directions (see figure 8 for the computational domain and the coordinate system). The entire computational domain is set to be $[0, 30h] \times [-10h, 10h]$ for the baseline cases, and a flow field as large as $[0, 10h] \times [-3h, 3h]$ is analysed in this study. Here, the grid resolution, the boundary conditions and other parameters are first determined such that unsteady simulations can be stably performed with the original Navier–Stokes solver, i.e. $\epsilon = 0$ in (4.4), except for the $Re = 4000$ case. At $Re = 4000$, the resolution is assured only based on the hybrid simulation. Details of the grid-dependence study are summarized in Appendix C together with the test for the exit-boundary condition. Importantly, the hybrid simulation is found to be rather insensitive to the grid resolution because the hybrid velocity field is continuously forced by the PTV data. Thus, the results solved with the 450×300 mesh are analysed in the following discussion.

A jet is ejected by imposing a top-hat velocity profile with hyperbolic-tangent functions at the boundary points on $x = 0$, as indicated in figure 8. Non-slip boundary conditions are imposed on the top and bottom walls as well as $x = 0$ except the nozzle exit. At the downstream boundary points, the convective boundary condition is imposed, where the convective velocity u_c is given by the averaged streamwise
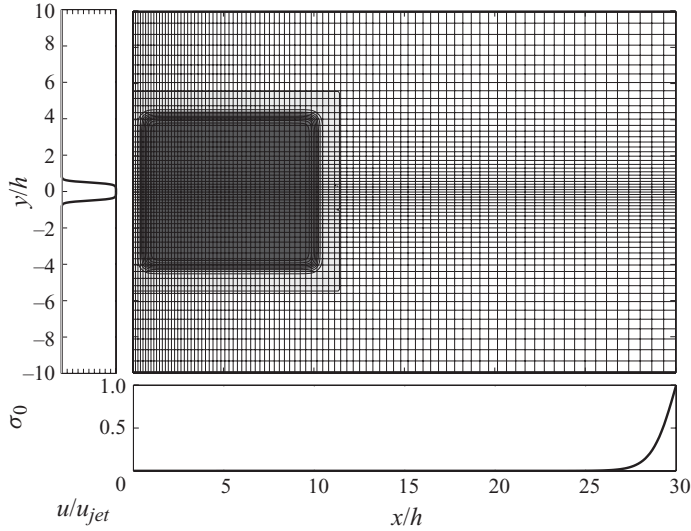
FIGURE 8. Computation mesh for the hybrid simulation (450×300, every five grid points) and contour of the patch function in a grey scale (interval of $\Delta f = 0.1$). Strength of the sponge term, σ_0 in (4.10), is drawn at the bottom, and the inlet-velocity profile is depicted on the left.

velocity along the exit line. To further suppress undesirable disturbances from the downstream boundary, a feedback term, the so-called 'sponge buffer zone', is added as shown in (4.10) so that the flow is forced to relax towards the uniform flow in $x/h \gtrsim 25$. The strength of the sponge term is drawn in figure 8. The influence of the domain size and the boundary conditions is assured by running the DNS for the same condition ($Re = 2000$) in a longer domain, $[0, 45h] \times [-10h, 10h]$, and the results are also listed in table 3 of Appendix C.

To actually feed the hybrid velocity field to the DNS, the intermediate velocity, $\hat{\boldsymbol{u}}$ in (4.11), is replaced by the linear combination given by (4.4). Accordingly, the rearrangement processes, (4.2) and (4.3), which are required for the PTV velocity field, are treated by the original Poisson equation so that an extra iteration process can be minimized. Here, since the domain in which PTV velocities are available is restricted by the size of the camera window, a so-called 'patch function', $f(x, y)$, is defined such that it takes unity in the middle of the camera window and gradually vanishes outside (see figure 8 for its contour). This function is multiplied by the PTV velocity field; therefore, the actual hybrid velocity field corresponding to (4.4) can be rewritten by

$$\begin{pmatrix} u \\ v \end{pmatrix}^{Hybrid} = [1 - \epsilon f(x, y)] \begin{pmatrix} u \\ v \end{pmatrix}^{DNS} + \epsilon f(x, y) \begin{pmatrix} u \\ v \end{pmatrix}^{PTV}. \quad (4.12)$$

When the PTV velocity field is overlaid with the patch function, its effect on the equation of continuity along the patch boundary can also be treated by solving the Poisson equation. Analysis of the convergence including the effect of the patch function was performed in Suzuki *et al.* (2009a). It should be noted that to calculate a pressure field, the Poisson equation (4.11) should be solved before superposing the PTV velocity component.
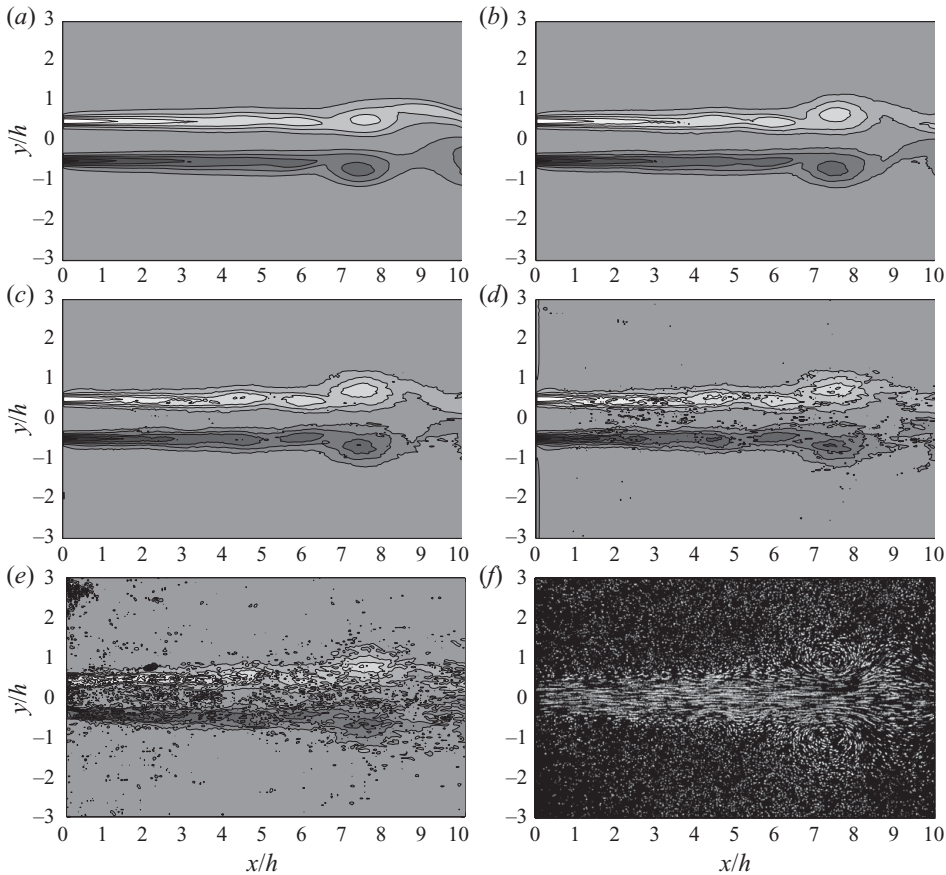
FIGURE 9. Comparison of vorticity contours at $Re = 1000$. (*a*) Hybrid simulation, $\epsilon = 0.08\Delta t^{PTV}$. (*b*) $\epsilon = 0.2\Delta t^{PTV}$. (*c*) $\epsilon = 0.5\Delta t^{PTV}$. (*d*) $\epsilon = 1.25\Delta t^{PTV}$. (*e*) PTV (10 frames are averaged). (*f*) Superposition of 10 consecutive images. Contour level: $-5 \leqslant \omega \leqslant 5$ with an interval of $\Delta\omega = 0.8$ for all contours, and counter-clockwise vorticity is drawn by lighter colours and clockwise one by darker colours. Time generation of all figures is the same as figure 7 (at $t = 90.8$, which is sufficient for the hybrid simulations to converge, as demonstrated in figures 10 and 13).

5. Features of hybrid simulation and comparison with experiments

5.1. *Basic features of the hybrid simulation*

To study the features of the hybrid simulation, we first observe velocity fields solved with the hybrid simulation and compare them with the PTV velocity field. Figure 9 exhibits typical vorticity contours of the hybrid simulation at $Re = 1000$ among different weights, ϵ in (4.12), and that directly computed from PTV at the same time generation. We also display superposition of ten consecutive frames from the high-speed camera to indicate particle trajectories for reference.

The hybrid vorticity fields in figure 9 show that the Kelvin–Helmholtz instability causes to generate nearly symmetric vortical structures in the shear layers. For a small weight on the PTV velocity field ($\epsilon = 0.08\Delta t^{PTV}$), the noise level is low, but small vortical structures seem to be unresolved. With increasing ϵ, the noise level is also increased, while distinctive vortex arrays are reconstructed. For the greatest weight ($\epsilon = 1.25\Delta t^{PTV}$), vortical structures can still be captured with a discernible noise level;
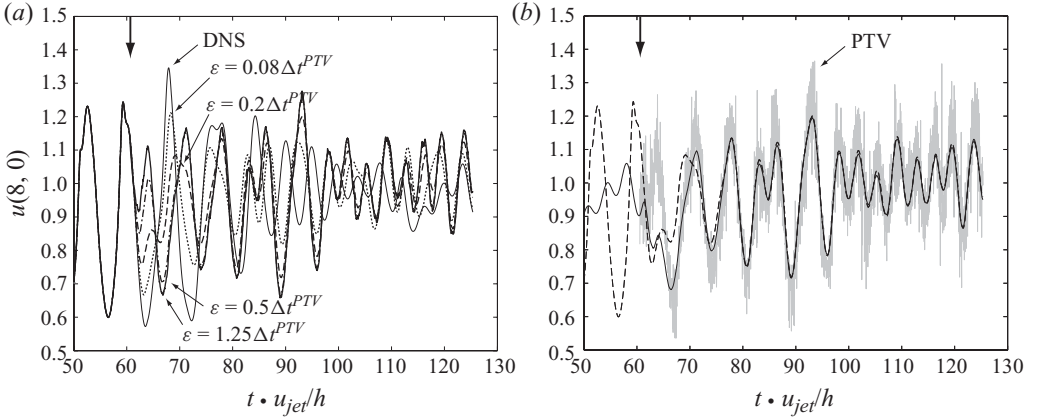
FIGURE 10. Time histories of the streamwise velocity at $(x/h, y/h) = (8, 0)$ for $Re = 1000$. Vertical arrow at $t = 60.6$ denotes the time at which the hybrid simulation is activated. (a) Comparison of different ϵ. Line patterns: $\cdots\cdots$, $\epsilon = 0.08\Delta t^{PTV}$; $- - -$, $\epsilon = 0.2\Delta t^{PTV}$; $-\cdot - \cdot-$, $\epsilon = 0.5\Delta t^{PTV}$; ———, $\epsilon = 1.25\Delta t^{PTV}$. Grey solid line denotes the DNS. (b) Comparison of different activation time. The dashed line denotes the case identical to (a) on the left ($\epsilon = 0.2\Delta t^{PTV}$). The solid line denotes the one activated later ($t = 126.0$) and shifted accordingly. The light grey line shows a time history directly computed from the PTV for reference.

in contrast, the vorticity field averaged over ten PTV frames barely exhibits vortical structures due to high-wavenumber noise although we can observe the correspondence between the PTV and hybrid vorticity fields.

Figure 10(a) compares the time histories of the streamwise velocity at $(x/h, y/h) = (8, 0)$ among different ϵ used in figure 9. For the first two highest weights (i.e. $\epsilon = 1.25\Delta t^{PTV}$ and $0.5\Delta t^{PTV}$), the time histories almost overlap rapidly although the one for the highest ϵ includes some high-frequency fluctuations. The next smaller case, $\epsilon = 0.2\Delta t^{PTV}$, slowly approaches the former two time histories, but does not overlap with them. The lowest case, $\epsilon = 0.08\Delta t^{PTV}$, follows neither any other hybrid time histories nor that of the original DNS.

Because the hybrid velocity field approaches the measured velocity field with sufficiently large ϵ, the result at later time should be independent of the initial condition. We run an additional case with $\epsilon = 0.2\Delta t^{PTV}$ by activating the hybrid simulation at $t = 126.0$ (at the end of the DNS time history in figure 10a). To compare this time history with the corresponding previous one, which is activated at $t = 60.6$, we accordingly shift the one that is activated later in figure 10(b) and also draw a time history directly computed from the PTV velocity field. These two hybrid time histories almost overlap about after two cycles of fluctuations; in fact, the standard deviation between them after $t = 80$ is only $0.006u_{jet}$. They also follow the PTV time history, which yet includes significant high-frequency noise. With sufficiently large ϵ, the hybrid velocity field appears to almost converge regardless of the initial velocity field. At the same time, it substantially reduces high-frequency noise in the PTV data.

In fact, we can clearly observe suppression of the high-frequency/wavenumber components in figure 11, which compares the frequency/wavenumber spectra of the streamwise velocity among the DNS, the hybrid simulation and the PTV. Figure 11(a) shows that the spectra of the PTV and the hybrid simulation agree well at low frequencies ($St \lesssim 0.3$). The local maximum ($St \approx 0.2$) roughly agrees with the most unstable frequency of the symmetric mode calculated from spatial linear stability
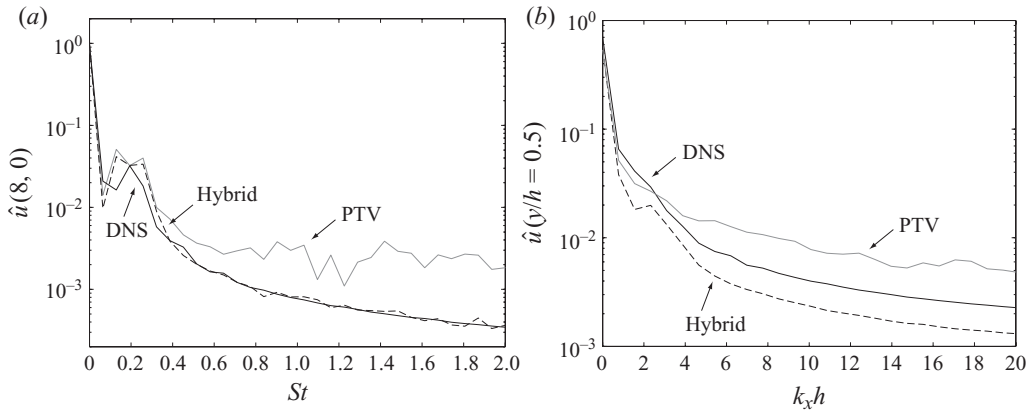
FIGURE 11. Comparison of the streamwise-velocity spectra among the DNS, the hybrid simulation ($\epsilon = 0.2\Delta t^{PTV}$) and the PTV at $Re = 1000$. (*a*) Frequency spectra. The time histories of $u(8, 0)$ in figure 10 are Fourier transformed. The time histories after $t = 78.9$ are segmented into three blocks, and the spectra are averaged using five samples with 50 % overlap. (*b*) Wavenumber spectra. The streamwise-velocity profiles along $y/h = 0.5$ in $1 \leqslant x/h \leqslant 9$ are Fouier transformed, and 40 snapshots are averaged for each case.

analysis ($St \approx 0.165$ at $x/h = 5$). With increasing frequency, the spectrum of the hybrid simulation then decays faster than that of the PTV and closely follows the DNS spectrum at $St > 0.5$. In contrast, the high-frequency components of the PTV spectrum hardly decay with frequency, and this is consistent with the high-frequency fluctuations observed in figure 10(*b*).

Similarly, the comparison of the wavenumber spectra in the shear layer in figure 11(*b*) shows that the hybrid simulation agrees with the PTV result only at low wavenumbers (e.g. the most unstable wavenumber of the symmetric mode is $k_x h \approx 1.8$ at $x/h = 5$ based on spatial linear stability analysis) and suppresses the high-wavenumber components relevant to the PTV velocity fields. Although the hybrid spectrum appears to decay with the wavenumber even faster than the DNS spectrum, the magnitude of the DNS streamwise velocity along $y/h = 0.5$ is somewhat greater than that of the PTV/hybrid simulation due to different shear-layer spreading rates. Thus, the results of the frequency/wavenumber spectra explain that the hybrid simulation can extract vortical structures in the shear layers by retaining resolvable-scale motion but with a lower noise level.

5.2. *Estimation of the necessary weight on the PTV velocity field*

Figure 9 has demonstrated that we can tune the signal to noise ratio by adjusting the weight on the PTV velocity field. As formulated in (4.8), the hybrid velocity field approaches that measured with the PTV over time as long as ϵ dominates over $\mathrm{Im}[\omega]\Delta t^{PTV}$. If we attempt to estimate the maximum global amplification rates using two-dimensional surrogate eigenfunctions computed in §2.2, they yield, for example, $\mathrm{Im}[\omega]_{max} \approx 0.31$ and 0.34 for the symmetric and asymmetric modes, respectively, at $Re = 1000$ (refer to Appendix B for the procedures). These amplification rates are yet somewhat higher than the threshold value deduced from figure 10(*a*), which is $\epsilon \approx 0.2\Delta t^{PTV}$.

To further explore the necessary condition for ϵ, we next impose the mode excited when the hybrid scheme has started. Taking a Fourier transform of the DNS velocity fields near the peak frequency, approximately $St \approx 0.13$ at $Re = 1000$, before the hybrid simulation is activated, we can extract dominant periodic fluctuations.
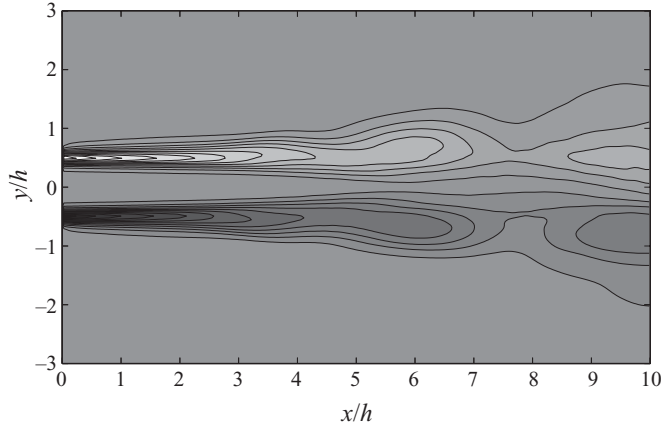
FIGURE 12. Vorticity contour of the disturbances extracted from the DNS ($Re = 1000$ and $St \approx 0.13$). Vorticity component is Fourier transformed during four periods of the target frequency, and the time-averaged vorticity is overlaid. Contour levels: $-5.0 \leqslant \omega \leqslant 5.0$ with an interval of $\Delta\omega = 0.4$, and the colour patterns are the same as figure 9.

Figure 12 depicts a streamwise-velocity contour of the extracted mode, which spatially grows in the domain of interest. Reducing its magnitude to the linear range ($|u'|_{max} \approx 0.01u_{jet}$), this mode is imposed as an initial condition superposed on the mean-velocity field, and the flow field is marched with the DNS (similar to the approach taken in Appendix B). Consequently, the amplification rate is estimated to be $\text{Im}[\omega]_{max} \approx 0.16$, which is consistent with the threshold weight deduced from figure 10(a).

The results of the estimated amplification rate of the entire system and the necessary condition for the PTV weight may be explained from the relation between the temporal and spatial growth rates. Referring to Gaster (1962), the temporal growth rate of instability waves can be converted to the spatial one. If this is applied to the current case, the temporal growth rate obtained in Appendix B is considered to be the maximum value, and it is decreased as the eigenfunction is spatially developed. The extreme case is the spatial eigenfunction, whose temporal growth rate vanishes. When we activate the hybrid scheme, spatially-developed disturbances dominate velocity fluctuations, and their temporal growth rate should be smaller than the maximum value given by the temporal eigenfunctions. As a result, the mode primarily excited at the time of activation governs the necessary weight on the PTV velocity field. Ideally, a spatial eigenfunction should not grow in time, but the extracted mode can initially grow because we have reduced its magnitude. In fact, even if we impose the mean flow without such a disturbance, the amplification rate changes only slightly. Although the mode extracted using a Fourier transform may not exactly measure the amplification rate of the actually excited mode, it is probably safe to assume that such an initial condition approximately derives the temporal amplification rate of the numerical system at the time of hybrid activation.

On the other hand, we can also evaluate the minimum weight on the PTV data from the hybrid simulations. In figure 13, we plot the time histories of

$$\mathcal{J}(t) \equiv \sum_{\substack{\text{All grid points}}} f^2(x, y)[(u^{Hybrid}(t, x, y) - u^{PTV}(t, x, y))^2$$

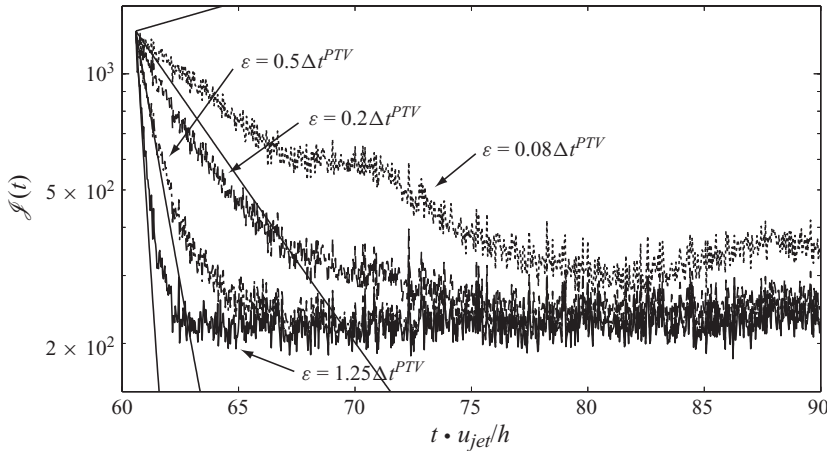$$+ (v^{Hybrid}(t, x, y) - v^{PTV}(t, x, y))^2] \quad (5.1)$$

FIGURE 13. Time histories of the discrete cost function given by (5.1). Line patterns are the same as those in figure 10(a). The decay rates estimated from (4.7) with $\text{Im}[\omega] = 0.1$ are also plotted using straight lines for all cases.

for various ϵ. This corresponds to the cost function (4.1) inside the patch in a discrete sense. For reference, we also draw the slopes of the estimated decay rates by setting $\text{Im}[\omega]_{max} = 0.1$ (which is found to be a reasonable fit) in (4.7). The time response becomes faster with increasing ϵ; in particular, the three cases, $\epsilon = 1.25\Delta t^{PTV}$, $0.5\Delta t^{PTV}$ and $0.2\Delta t^{PTV}$, seem to reach similar stationary states within the sampling period. These trends are consistent with the time histories of streamwise velocity in figure 10(a). On the other hand, the hybrid simulation with $\epsilon = 0.08\Delta t^{PTV}$ represents neither two-dimensional simulation nor experimental flow field due to an insufficient weight on the PTV data. In fact, if the global amplification rate is greater than $\text{Im}[\omega]_{max} = 0.1$, (4.7) indicates that it does not converge, as shown by one straight line increasing in figure 13.

The amplification rate crudely estimated from figure 13, $\text{Im}[\omega] = 0.1$, is somewhat smaller than that extracted from the DNS, which is $\text{Im}[\omega] \approx 0.16$. The difference may be due to several assumptions used to derive (4.7). Nonetheless, the aforementioned estimate from the DNS seems to be sufficient in a sense that the hybrid velocity field approaches the measured one; namely the estimate is, at least, on the safer side. In fact, the weight ϵ, which is twice the amplification rate, i.e. $r = \exp\left(-2\text{Im}[\omega]\Delta t^{PTV}\right)$, theoretically minimizes the error given by (4.7) as $n \to \infty$ for $\text{Im}[\omega] > 0$.

For general Navier–Stokes solvers, high-wavenumber disturbances satisfy $\exp(\text{Im}[\omega]\Delta t) < 1$. This helps suppress the noise components associated with the measurement errors, $\boldsymbol{w}$, which are amplified with differentiation. On the other hand, physical instability modes with low wavenumbers grow in general Navier–Stokes solvers; however, even these physical instabilities are not self-driven under a sufficiently large weight on the PTV data in the hybrid simulation. For example, the two-dimensional Kelvin–Helmholtz instability predicted by the original Navier–Stokes solver should decay in the hybrid simulation. But instead, flow instabilities excited in the experiments are reconstructed in the hybrid simulation, as the error parts are diminished in the course of time. Hence, strong organized structures that are typically excited in two-dimensional simulations tend to be suppressed in the hybrid
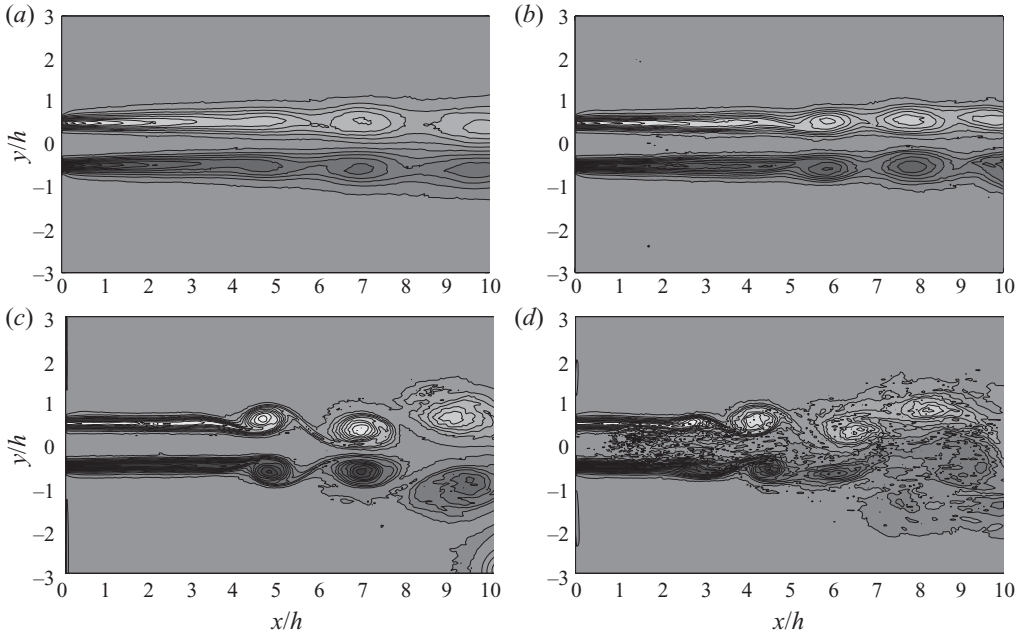
FIGURE 14. Comparison of vorticity contours at different Reynolds numbers ($\epsilon = 0.2 \Delta t^{PTV}$). (*a*) $Re = 500$. (*b*) $Re = 1000$. (*c*) $Re = 2000$. (*d*) $Re = 4000$. Contour level: $-5 \leqslant \omega \leqslant 5$ with an interval of $\Delta \omega = 0.4$ for all contours, and counter-clockwise vorticity is drawn by lighter colours and clockwise one by darker colours.

simulation, and the flow field appears to be rather governed by three-dimensional fluid dynamics (see Suzuki *et al.* 2009*a* for detailed discussion).

5.3. *Reynolds-number dependence and the necessary weight*

We now discuss the effects of the Reynolds number on the hybrid simulation. Figure 14 displays typical vorticity contours calculated with the hybrid simulation at different Reynolds numbers. Here, we set the weight to be $\epsilon = 0.2 \Delta t^{PTV}$ for all cases. As the Reynolds number increases, the vorticity becomes stronger and intensive braid regions appear more upstream. Moreover, laminar vortical structures start collapsing and the measurement noise level increases at higher Reynolds numbers.

Such changes can increase the necessary weight on the PTV velocity field, ϵ, in the hybrid algorithm at least in two ways. One is due to three-dimensional motions, which may be relevant in the braid region (Williamson 1996) and the vortex core (Rogers & Moser 1992). Deviation of motion from the continuity in two dimensions causes the cost function to increase constantly, as discussed in Suzuki *et al.* (2009*a*). The other is the limitation of the PTV resolution. Once the scales of eddies become smaller than the resolvable scale of the PTV, they amplify measurement errors, and the DNS solver cannot resolve such motion well even if the physical scale is still resolvable with the original DNS. This also elevates the cost function, possibly resulting in a larger necessary weight on the PTV velocity field.

Table 2 lists the estimated amplification rates of the entire numerical system at the different Reynolds numbers. We estimate them by imposing the extracted mode in the DNS and also by fitting slopes with the time histories of the cost functions, as explained in figures 12 and 13, respectively; hence, the values, particularly the latter

Case	Re	$N \ (\equiv \Delta t^{PTV}/\Delta t^{DNS})$	$\mathrm{Im}[\omega]_{max}^{DNS}$	$\mathrm{Im}[\omega]_{max}^{Hybrid}$
A	500	5	0.06	0.1
B	1000	5	0.16	0.1
C	2000	5	0.24	0.15
D	4000	8	(0.26)	0.2

TABLE 2. Comparison of the amplification rates for the entire system at different Reynolds numbers. The fourth column denotes the values estimated by imposing the mode excited in the DNS (cf. figure 12), and the fifth column those estimated from the slopes of the cost functions (cf. figure 13). The excited mode in the DNS at $Re = 4000$ is extracted beyond the time of hybrid activation; accordingly, the estimate is uncertain.

ones include large uncertainties. Although the estimate from the slopes of the cost function tends to be lower than the estimate using the DNS, their magnitudes are similar. More importantly, both results suggest that the necessary weight becomes greater with increasing Reynolds number. In general, linear stability analysis derives that the growth rate depends less on the Reynolds number at $Re \gtrsim 1000$, namely in the inviscid limit. However, table 2 indicates that the necessary weight can increase as much as 50 % from $Re = 1000$ to 2000, and our previous study on flows past an airfoil (Suzuki *et al.* 2009*b*) also implied a rapid increase of $\mathrm{Im}[\omega]_{max}$ with Re. As discussed in §5.2, the disturbances at the time of hybrid activation are rather close to spatially developed instability waves, whose growth rate is smaller than the maximum growth rate of temporal eigenfunctions. In addition, three-dimensional motions and measurement noise due to smaller eddies can contribute to greater amplification rates, as discussed above. Hence, it is understandable that the necessary weight increases with the Reynolds number.

5.4. *Comparison with an experiment*

There were relatively few experimental studies of planar jets in the Reynolds-number range of our interest in the past (Sato 1960; Sfeir 1979). Sato (1960) reported both mean-flow and fluctuating quantities in detail at $Re \approx 4000$. Referring to his results, we observe statistical flow properties of planar jets solved with the hybrid simulation in this section. In our experiment, the memory of the high-speed camera restricted the sampling period of the image measurement, and we start processing flow images soon after the jet becomes stationary but before the jet starts bending towards the wall. Therefore, the results of the hybrid simulation are statistically limited. However, by comparing them with an independent experiment, we demonstrate that the samples taken in this study retain fundamental characteristics of an unstable planar jet and support the generality of the current analysis about instability waves.

In the following, we refer to a case in Sato (1960) where an air jet was issued with the centreline exit velocity of $u_{C.L.} = 10.0$ m s^{-1}. In his experiment, a rectangular exit of $h = 6$ mm height times $w = 400$ mm spanwidth is followed by a straight-channel part of $l = 1100$ mm length. In contrast, in our experiment, the section-averaged velocity is defined as u_{jet}, and the jet was ejected immediately from a converging nozzle. Therefore, the shear-layer thickness and the section-averaged flow rate may be different in a non-dimensional sense between the two experiments. For calibration of the transverse length scale, the streamwise-velocity profile in Sato (1960) at $x = 30$ mm is integrated to estimate the flow rate, and the exit height is redefined as $h \equiv \int \bar{u}(y)\mathrm{d}y/u_{C.L.}$ in the following comparison.
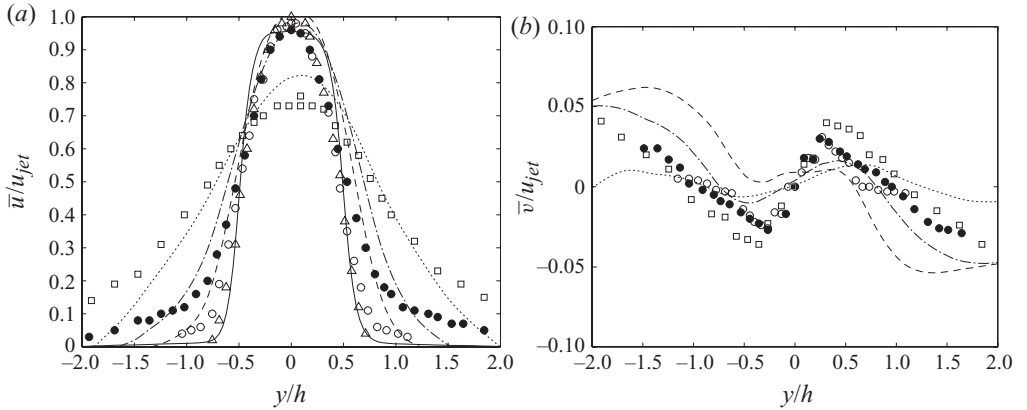
FIGURE 15. Comparison of the time-averaged velocities between the hybrid simulation ($\epsilon = 0.5\Delta t^{PTV}$) and the experiment (Sato 1960) at $Re \approx 4000$. (a) Streamwise velocity. (b) Transverse velocity. Lines represent the hybrid simulation and the symbols the experiment: ——, $\triangle$, $x/h = 1.67$; — — —, $\bigcirc$, $x/h = 5.0$; — · — · —, $\bullet$, $x/h = 6.67$; · · · · ·, $\square$, $x/h = 10.0$.

We first observe mean-flow properties. Setting $\epsilon = 0.5\Delta t^{PTV}$, we ensure that the PTV velocity field governs the hybrid simulation at $Re = 4000$. Figure 15(a) compares streamwise-velocity profiles at several downstream stations. The velocity gradients near the nozzle exit of Sato's experiment (Sato 1960) are gentler than those in the hybrid simulation, probably because the shear layers are thicker owing to boundary-layer development along the long channel. In fact, he reported that the velocity profile for this case was close to a parabolic shape. Nonetheless, the diffusive rates just outside the shear layers appear to be similar between the two results, and the centreline velocities agree reasonably well.

Likewise, figure 15(b) plots transverse-velocity profiles. Because of the limited sampling period in the hybrid simulation, the offset of the centreline (i.e. asymmetry) is discernible. The gradients outside the shear layers between the two results are relatively close at $x/h = 5.0$ and 6.67, indicating that the hybrid simulation captures suction flow. But, the gradients near the centreline in the hybrid simulation are lower than that of Sato's profiles (Sato 1960). As shown in figure 15(a), the streamwise-velocity profile of the hybrid simulation is similar to a top-hat shape, while Sato's profile is closer to a parabola. This can change the spreading rate of the jet in the potential core, leading to different transverse-velocity gradients near the centreline.

Next, we analyse streamwise-velocity fluctuations. Figure 16(a) shows that the sectional profiles depict similar double-hump shapes for both results, but the corresponding downstream sections differ significantly. In fact, the comparison of the centreline profiles in figure 16(b) reveals that the initial disturbance level is about one order of magnitude higher in the hybrid simulation; subsequently, both profiles exponentially grow with similar growth rates. The fluctuations in the hybrid simulation saturate before $x/D = 10$, while those of Sato's experiments monotonically grow up to $x/D \approx 12$. In his experiment, the nozzle exit was followed by a long channel and initial disturbances were carefully minimized. In contrast, a straight convergent nozzle is used for the current study to emphasize vortical structures; therefore, it is understandable that vortical structures are developed more upstream in our study.
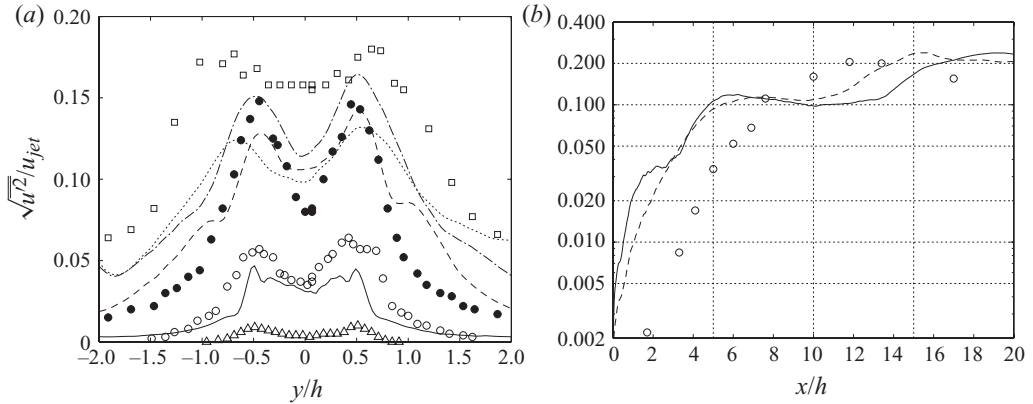
FIGURE 16. Comparison of the time-averaged streamwise-velocity fluctuation between the hybrid simulation and an experiment (Sato 1960) at $Re \approx 4000$. (a) Sectional profiles ($\epsilon = 0.5\Delta t^{PTV}$). Line patterns and symbols are the same as figure 15. (b) centreline profiles. Hybrid simulation: $- - -$, $\epsilon = 0.2\Delta t^{PTV}$; ———, $\epsilon = 0.5\Delta t^{PTV}$. Experiment (Sato 1960) is denoted by $\bigcirc$.

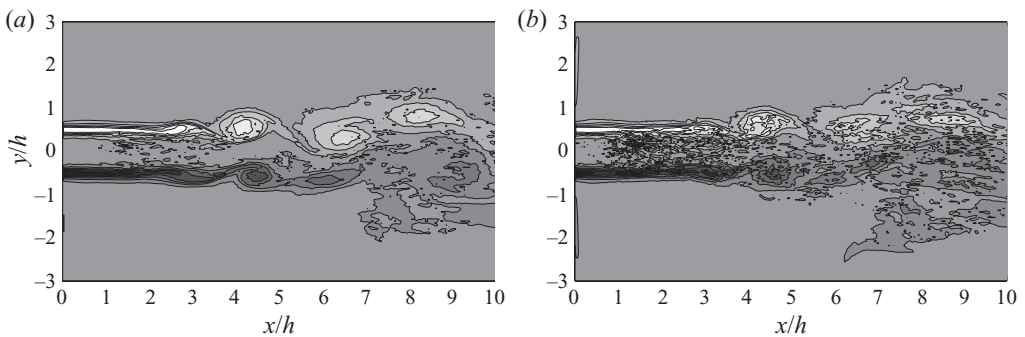FIGURE 17. Comparison of vorticity contours from the hybrid simulation ($Re = 4000$). (a) $\epsilon = 0.2\Delta t^{PTV}$. (b) $\epsilon = 0.5\Delta t^{PTV}$. Time generations are the same. Contour levels: $-5.2 \leqslant \omega \leqslant 3.6$ with intervals of $\Delta\omega = 0.8$, and the colour patterns are the same as figure 9.

We notice in figure 16(b) that the hybrid profile with the higher PTV weight (i.e. $\epsilon = 0.5\Delta t^{PTV}$) depicts a hump up to $x/h \lesssim 3$ relative to the one with $\epsilon = 0.2\Delta t^{PTV}$, and the rest of the growing part up to $x/h \lesssim 10$ agrees better each other. This hump corresponds to measurement noise of the PTV. Figure 17 compares instantaneous vorticity contours between the two weights at the same time generation. The one with the higher weight ($\epsilon = 0.5\Delta t^{PTV}$) includes significant high-wavenumber noise in the potential core. From these results, we can deduce that when the magnitude of initial instability waves is comparable to or lower than the measurement noise level, it is difficult to suppress the later, particularly at higher Reynolds numbers, in which the viscous-dissipation effect is limited. Once organized structures are developed, their disturbance level relative to the measurement noise is increased, and flow structures can be clearly captured.

6. Analysis of Kelvin–Helmholtz instability waves

We finally analyse instability waves using bi-orthogonal decomposition. We select the case at $Re = 1000$ with the weight of $\epsilon = 0.2\Delta t^{PTV}$, where the noise level is low, but

convergence of hybrid velocity fields has been confirmed in §§ 5.1 and 5.2. Moreover, large-scale vortical structures are formed downstream.

Since the Kelvin–Helmholtz instability waves are expressed as eigenfunctions in the frequency domain, hybrid velocity fields, (u, v), are Fourier-transformed in time at a designated frequency with the Hann window, and they are denoted by $(\hat{u}, \hat{v})$ after normalization. By substituting $\int \hat{u}\,\mathrm{d}y$ into Ψ in (2.6), the coefficients of both symmetric and asymmetric modes can be calculated at each station. Here, the streamwise-velocity profile for the Orr–Sommerfeld operators, $U(y)$, is calculated by averaging it only during the sampling period of the Fourier transform.

Calculation of bi-orthogonal decomposition can be verified using the orthogonality between the symmetric and asymmetric eigenfunctions, but there is no rigorous way to prove that the calculated coefficient exactly extracts the amplitude of instability waves for a full unsteady flow field. Yet, we refer to three quantities for indicators below. The first is a coefficient calculated with the least squares minimization between an eigenfunction and a stream function in the frequency domain. Such a coefficient is given by

$$ b_m \equiv \frac{\sum_1^{N_y+1} \psi_m^* \psi}{\sum_1^{N_y+1} \psi_m^* \psi_m}, \qquad (6.1) $$

where again $\psi \equiv \int \hat{u}\,\mathrm{d}y$, and the summation is taken over all the grid points in the transverse direction (the approach is analogous to the one taken by Suzuki & Colonius 2006). The second is Fourier-transformed velocity components along the centreline, as $\hat{u}(y=0)$ is relevant to the symmetric mode and $\hat{v}(y=0)$ to the asymmetric one. The last is a surrogate eigenfunction given by (2.12) for a spatial problem; namely complex wavenumbers of eigenfunctions are integrated in the streamwise direction.

We start with a simple case to demonstrate the feasibility of the approaches explained above. From figure 11(*a*), we select the centre of the peak frequency ($St = 0.206$) and take a Fourier transform of the hybrid velocity field for a long period (10 periods of the peak frequency centred at $t = 90.8$ in figure 10). Figure 18 depicts the amplitude profiles of eigenfunctions extracted from such a Fourier-transformed velocity field, one being calculated with bi-orthogonal decomposition (2.6) and the other with the least squares minimization (6.1). For reference, the surrogate eigenfunctions and the centreline velocities in the frequency domain are also plotted. We do not expect that (2.6) and (6.1) coincide with each other because actual unsteady velocity fields include modes other than discrete solutions in linear stability analysis. Nonetheless, they reasonably agree in the region in which the disturbances grow exponentially. When they start saturating or locally dent, the profiles of bi-orthogonal decomposition drop more sensitively than those of the least squares minimization.

Figure 18 also indicates that the growth rate of the extracted symmetric eigenfunction follows the prediction by linear stability analysis (i.e. symmetric surrogate eigenfunction) downstream. For the asymmetric mode, the extracted growth rate is somewhat lower than the prediction. The linear stability analysis actually estimates a higher spatial growth rate for the asymmetric mode than the symmetric one. However, probably because the sampling period was shortly after the impulsive start of the jet, the symmetric mode was still dominant. In order to obtain good agreement in the streamwise evolution between experimental data and surrogate eigenfunctions, we may need to sample the data for a much longer period. In the
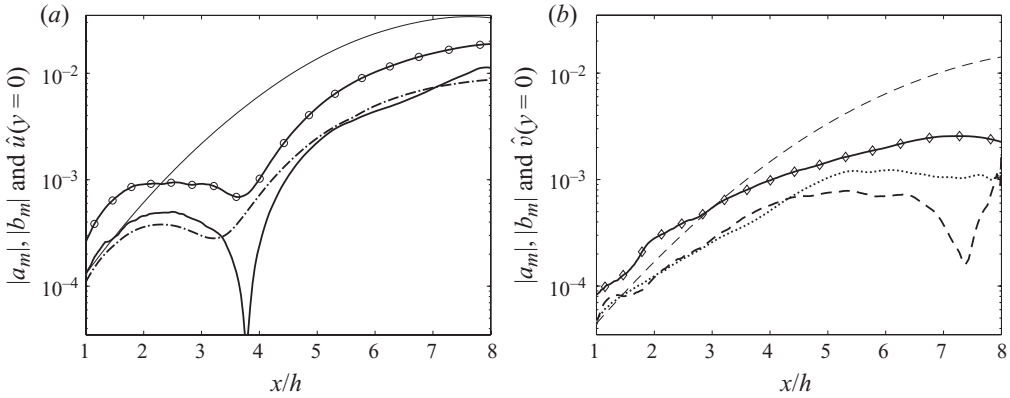
FIGURE 18. Streamwise evolution of the eigenfunctions and the Fourier-transformed velocity components along the centreline at $St = 0.206$ during 10 periods ($Re = 1000$). (*a*) Symmetric components. Amplitudes of the stream function: —— (thicker), bi-orthogonal decomposition (2.6); $- \cdot - \cdot -$ (thicker), least squares minimization (6.1). Surrogate eigenfunction: —— (thinner). Fourier-transformed streamwise velocity: $-\circ-\circ-$, $\hat{u}(y = 0)$. (*b*) Asymmetric components. Amplitudes of the stream function: $- - -$ (thicker), bi-orthogonal decomposition (2.6); $\cdots\cdots$ (thicker), least squares minimization (6.1). Surrogate eigenfunction: $- \ - \ -$ (thinner). Fourier-transformed transverse velocity: $-\diamond-\diamond-$, $\hat{v}(y = 0)$.
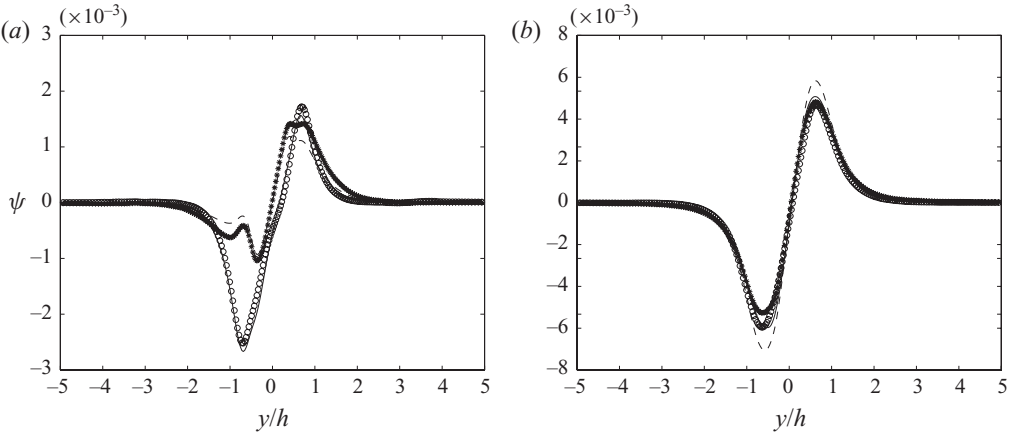

FIGURE 19. Comparison of the Fourier-transformed stream functions (during 10 periods) at $St = 0.206$ ($Re = 1000$). (*a*) $x/h = 5.0$. (*b*) $x/h = 7.5$. Lines denote the eigenfunction extracted using bi-orthogonal decomposition: ——, real part; $- - -$, imaginary part. Symbols denote the original stream function from the hybrid simulation: $\circ$, real part; $*$, imaginary part.

following discussion, we remove the profiles of surrogate eigenfunctions, which are relevant only in a statistical sense.

We then compare the sectional eigenfunctions with the stream functions from the hybrid simulation in the frequency domain at two streamwise locations in figure 19. Here, we determine the complex amplitudes of the eigenfunctions based on bi-orthogonal decomposition. At both locations, they agree fairly well in magnitude and phase although the flow may become nonlinear downstream (e.g. the magnitude of velocity fluctuations is $\sqrt{\overline{u'^2 + v'^2}} \approx 0.11 u_{jet}$ at $x/h = 7.5$).
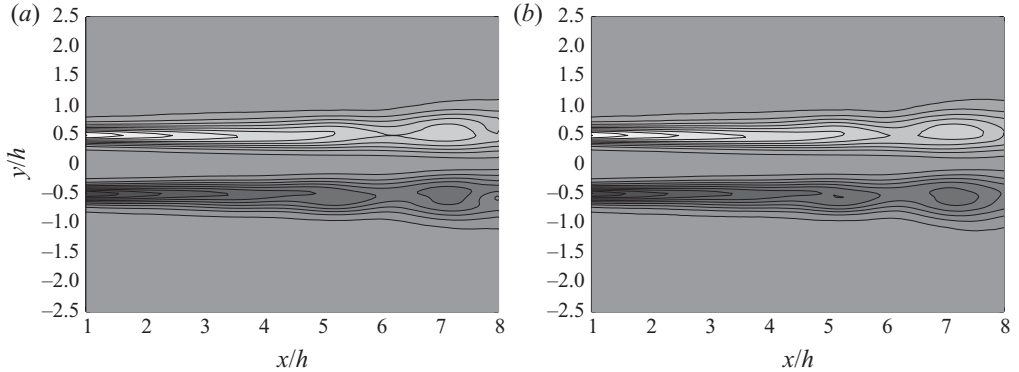
FIGURE 20. Vorticity fields of the Fourier-transformed velocity during ten periods at $St = 0.206$ ($Re = 1000$). (*a*) Reconstructed contour with bi-orthogonal decomposition. (*b*) Contour directly obtained from Fourier transform of the hybrid velocity field. The real part of the vorticity field is superposed on the mean vorticity field for both contours. Contour levels and colour patterns are the same as figure 14.

Figure 20(*a*) draws a vorticity field reconstructed using these amplitudes and eigenfunctions in bi-orthogonal decomposition, and figure 20(*b*) also displays the original vorticity field at the corresponding frequency. The reconstructed vorticity field captures both magnitude and phase over the entire extent shown in the figure. Beyond $x/h = 8$, where the velocity profile significantly diffuses, it is difficult to identify the most unstable physical mode in a spatial problem using the spectral method. But, these results demonstrate that bi-orthogonal decomposition is applicable to hybrid velocity fields at the peak frequency by taking a Fourier transform for a long sampling period.

To further emphasize the benefit of low measurement noise in the hybrid velocity fields, we reduce the period of Fourier transform so that we can readily tag the phase of vortical structures in the time domain. Taking two periods of the target frequency, $St = 0.206$, centred at $t = 109.0$ in figure 10, figure 21 similarly plots the amplitude profiles of eigenfunctions together with Fourier-transformed velocities at the centreline. In both symmetric and asymmetric components, amplitudes calculated by the two approaches show decent agreement over the entire extent. Moreover, the sectional eigenfunctions represent the stream functions quite well at the two stations in figure 22.

Applying the same approach at the subharmonic frequency ($St = 0.103$), we similarly plot the streamwise amplitude profiles and the sectional eigenfunctions in figures 23 and 24, respectively. The streamwise-velocity component once decreases in $4 \lesssim x/h \lesssim 6$ in figure 23(*a*); accordingly, the profile of bi-orthogonal decomposition sharply drops, yet its phase seems to deviate from the other profiles. In contrast, the asymmetric components almost exponentially grow all together and depict relatively smooth profiles during this sampling period. The agreement between the eigenfunction and the stream function at $x/h = 5$ is actually poor, while that at $x/h = 7.5$ appears to be better.

At the harmonic frequency ($St = 0.413$), we can observe the same trends in figure 25 (we stop calculating the amplitudes beyond $x/h \approx 5.6$ due to the aforementioned difficulty in the spectral method). Here, we also observe a sharp trough in the asymmetric profiles as the disturbances start saturating. In fact, the comparison between the eigenfunction and the stream function at $x/h = 5.0$ exhibits discrepancy
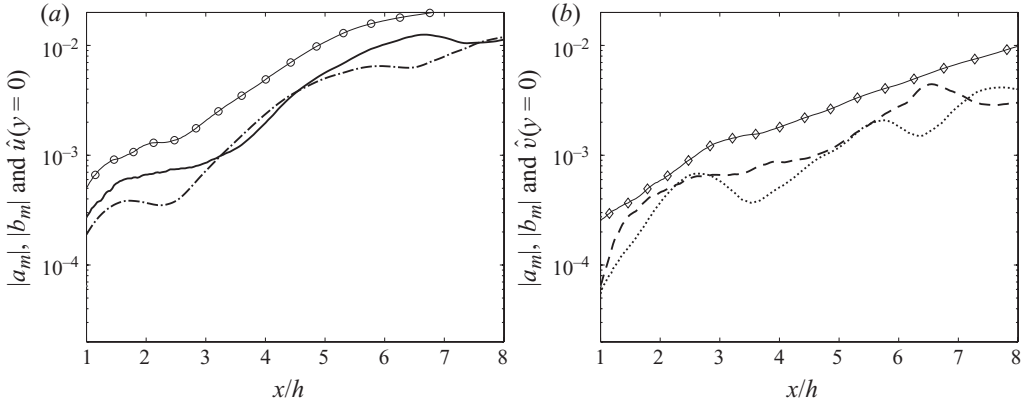
FIGURE 21. Streamwise evolution of the eigenfunctions and the Fourier-transformed velocity components along the centreline at $St = 0.206$ for two periods ($Re = 1000$). (a) Symmetric components. (b) Asymmetric components. Line patterns and symbols are the same as figure 18.
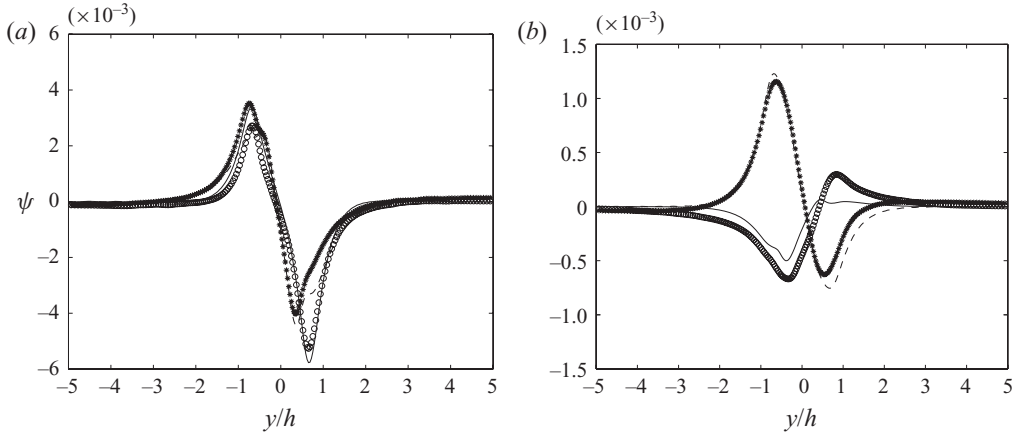

FIGURE 22. Comparison of the Fourier-transformed stream functions for two periods at $St = 0.206$ ($Re = 1000$). (a) $x/h = 5.0$. (b) $x/h = 7.5$. Line patterns and symbols are the same as figure 19.

in figure 26(b). They rather agree better upstream ($x/h = 2.5$) in figure 26(a). As the frequency increases, the growth rate of instability waves peaks more upstream. This explains the better agreement upstream at the harmonic and downstream at the subharmonic.

Finally, we attempt to reconstruct an instantaneous vorticity field using bi-orthogonal decomposition. By extracting amplitudes of eigenfunctions near the peak frequency with an half-octave interval (i.e. $St = 0.103$, 0.146, 0.206 and 0.290), we compute the Fourier-transformed velocity field at each frequency and superpose them together with the mean velocity field. Figure 27 compares the real part of the superposed vorticity field with the instantaneous one at $t = 109.0$, which is the centre during the two periods of the sampling frequency. Because the sampling period is relatively short even at $St = 0.103$, the real part of the reconstructed vorticity field captures the instantaneous field, which yet includes disturbances other than specified instability waves. Both magnitude and phase of the vorticity field agree well
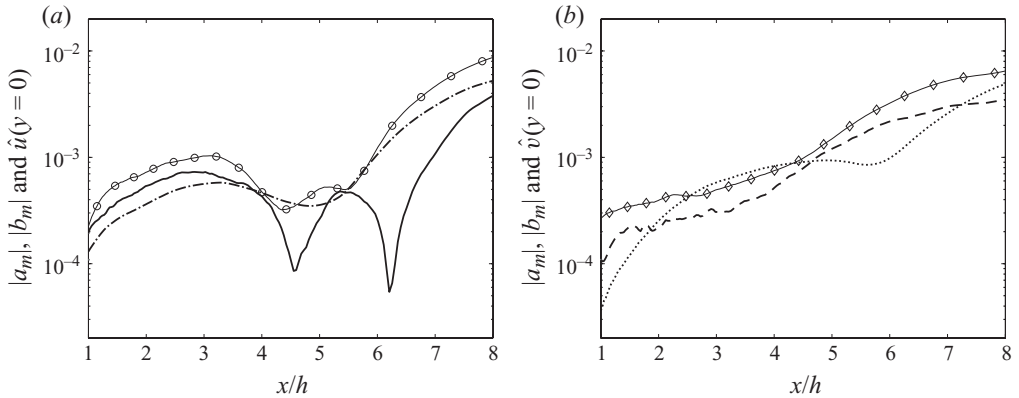
FIGURE 23. Streamwise evolution of the eigenfunctions and the Fourier-transformed velocity components along the centreline at $St = 0.103$ for two periods ($Re = 1000$). (*a*) Symmetric components. (*b*) Asymmetric components. Line patterns and symbols are the same as figure 18.
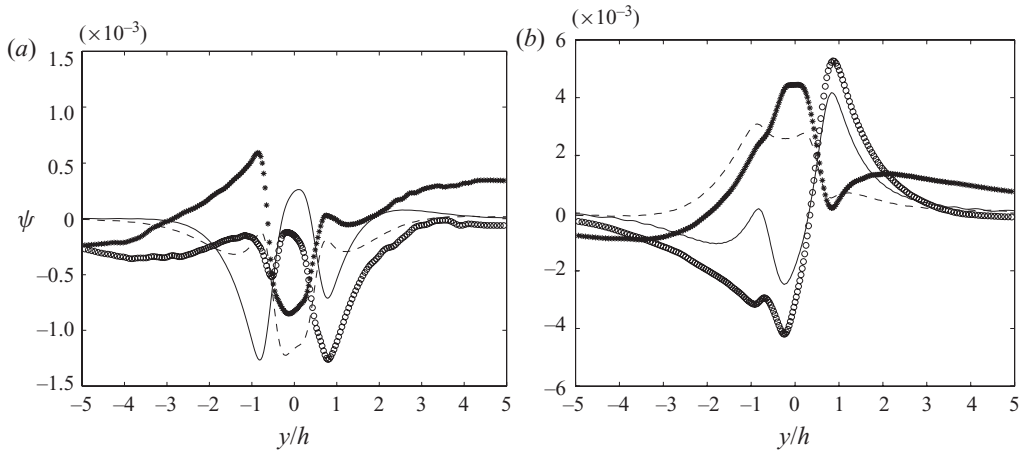

FIGURE 24. Comparison of the Fourier-transformed stream functions for two periods at $St = 0.103$ ($Re = 1000$). (*a*) $x/h = 5.0$. (*b*) $x/h = 7.5$. Line patterns and symbols are the same as figure 19.

in most of the extent, but the agreement deteriorates with downstream distance. In particular, the eigenfunction at $St = 0.290$ exhibits noticeable discrepancy with the original Fourier-transformed stream function from the hybrid simulation (not shown). To accurately extract instability waves over a range of frequencies, we may need to decompose the velocity field into the mean flow, large-scale coherent structures and small-scale disturbances (Reynolds & Hussain 1972), which requires a closer model for the Reynolds stress. Nonetheless, the overall agreement in this test demonstrates that the hybrid simulation is capable of analysing instantaneous unsteady velocity fields quantitatively.

7. Conclusions

We have introduced hybrid unsteady-flow simulations combining PTV and DNS to investigate planar-jet flows at low Reynolds numbers ($Re = 500$–4000) and
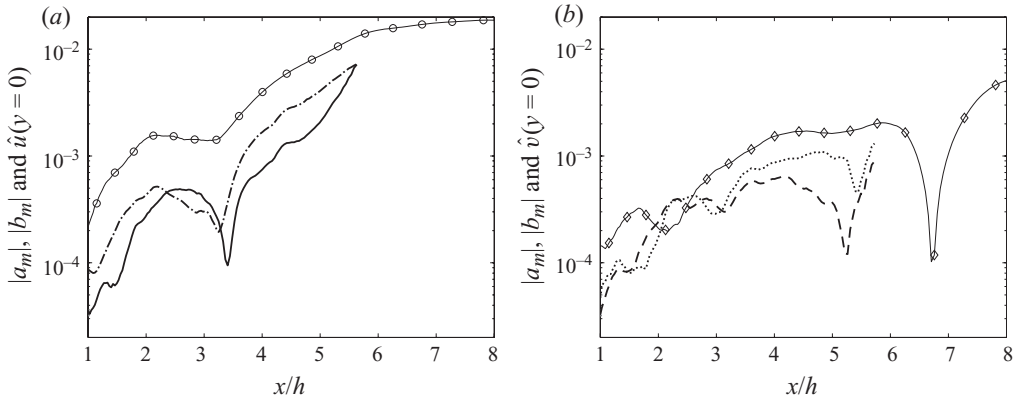
FIGURE 25. Streamwise evolution of the eigenfunctions and the Fourier-transformed velocity components along the centreline at $St = 0.413$ for two periods ($Re = 1000$). (a) Symmetric components. (b) Asymmetric components. Line patterns and symbols are the same as figure 18.
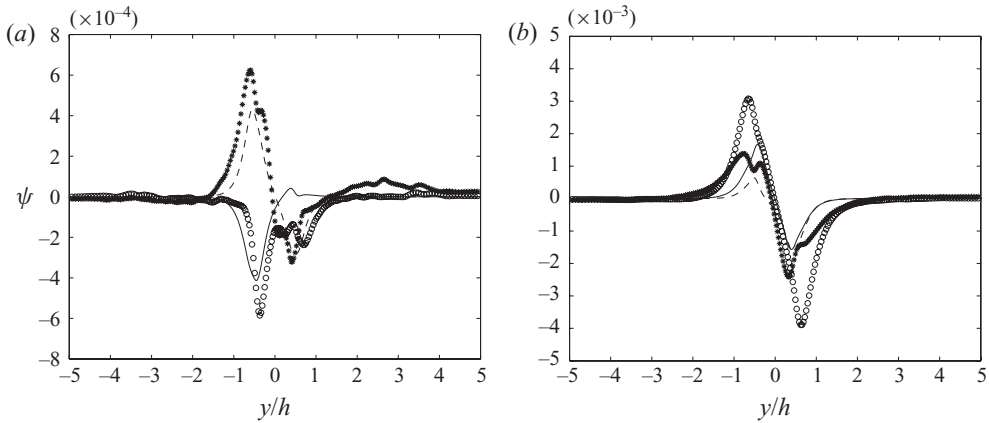

FIGURE 26. Comparison of the Fourier-transformed stream functions for two periods at $St = 0.413$ ($Re = 1000$). (a) $x/h = 2.5$. (b) $x/h = 5.0$. Line patterns and symbols are the same as figure 19.
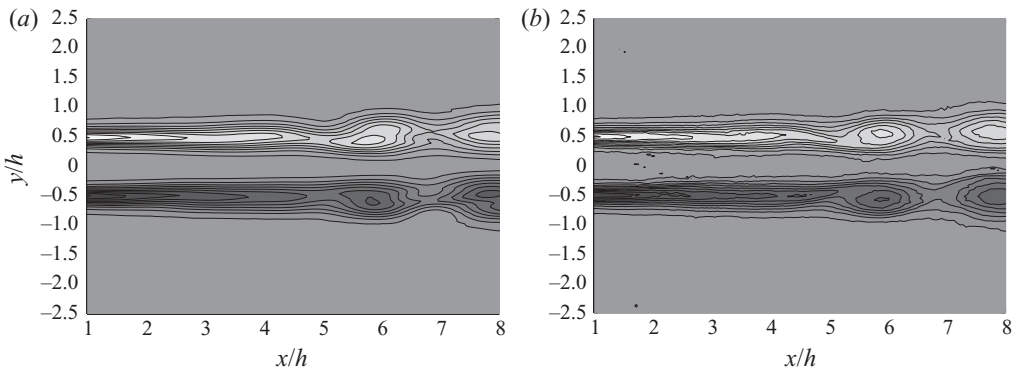

FIGURE 27. Comparison of the vorticity fields ($Re = 1000$ at $t = 109.0$). (a) Reconstruction by superposition of the eigenfunctions calculated with bi-orthogonal decomposition ($St = 0.103$, 0.146, 0.206 and 0.290). (b) Instantaneous vorticity field computed with the hybrid simulation at the corresponding time. Contour levels and colour patterns are the same as figure 14.

demonstrated its capabilities by analysing the Kelvin–Helmholtz instability waves using bi-orthogonal decomposition. We have conducted time-resolved PTV in a water tunnel and acquired unsteady jet flows on a laser sheet. By synchronizing a multiple of the computational time step, $N\Delta t^{DNS}$, with the frame rate of the PTV system, Δt^{PTV}, we keep supplying the PTV velocity field to the two-dimensional DNS solver in the course of time. To be precise, we recast the PTV velocity field in a least squares sense to satisfy the equation of continuity and linearly combine it with the velocity field updated with the DNS at every N time steps. The weight between the PTV and DNS velocity fields is determined so that the flow field is gradually converged to that of the PTV. As a result, a series of unsteady velocity fields that temporally and spatially satisfy the governing equations can be obtained with the resolution comparable to the DNS but the noise level much lower than that of the original PTV velocity fields.

The key parameter in the hybrid algorithm is the weight between the PTV and DNS velocity fields. We can suppress the measurement-noise level by reducing the weight on the PTV velocity field, but it must be greater than the threshold value associated with the amplification rate of the entire numerical system. We have estimated the necessary weight by computing the convergence rate of the hybrid velocity field and deduced that it is determined by the amplification rate of the initial velocity field given by the DNS. On the other hand, the maximum growth rates of temporal eigenfunctions calculated with the locally-parallel-flow assumption are estimated to be higher than the amplification rate of the initial velocity field. The actual disturbances are spatially developed in a spreading jet when the hybrid algorithm is activated; accordingly, their effective growth rates are likely smaller than those of the temporal eigenfunctions. The necessary weight is also found to be increased with increasing Reynolds number. This may be caused by the spanwise motion and the measurement-noise level rather than the viscous effect of the Kelvin–Helmholtz instability.

To demonstrate one of the capabilities of the hybrid simulation, namely the spatial and temporal filtering, we have analysed the Kelvin–Helmholtz instability based on bi-orthogonal decomposition. Because this approach requires high-order spatial derivatives, it is challenging to apply it for time-resolved velocity data contaminated with measurement noise. Assuming the mean flow to be locally parallel and transversely sheared, symmetric and asymmetric eigenfunctions from linear stability analysis have been extracted near the most unstable frequency, $St \approx 0.1$–0.4. The inner product of a spatial problem for a non-self-adjoint system has been used to determine the amplitude of instability waves at each downstream station, and the evolutions of both symmetric and asymmetric modes have been compared with those given by the least squares minimization as well as Fourier-transformed velocity components along the centreline. In addition, a vorticity field has been reconstructed from superposition of these extracted eigenfunctions at several frequencies, and the phase and magnitude of the vorticity field have been compared with the original hybrid velocity field. Through these tests, the resolution and the noise level of the hybrid velocity fields are shown to be acceptable for quantitative analysis of unsteady velocity fields, even in an instantaneous sense.

The analysis based on bi-orthogonal decomposition has suggested that eigenfunctions from linear stability analysis represent local velocity fluctuations well in the regions in which the spatial growth rate is relatively high. Namely, sectional stream functions extracted from the hybrid simulation agree with the eigenfunctions, and the agreement is better downstream at the low frequency and upstream at the high frequency. Such a trend is consistent with the fact that instability waves saturate more upstream with increasing frequency. On the other hand, the streamwise

growth of instability waves extracted with Fourier transform for a short period does not necessarily follow the growth rate of the spatial eigenfunction. Correlated length scales of disturbances are limited in the streamwise extent during a short time period. To acquire good agreement between velocity measurement and linear stability analysis for the streamwise evolution, decomposition of mean flow, large-scale coherent modes and small-scale fluctuations may be required, and many ensembles are probably necessary.

Appendix A. Galerkin method using Jacobi polynomials

As mentioned in §2.3, the Orr–Sommerfeld equation is solved using the Galerkin method with the Jacobi polynomials of $(\alpha, \beta) = (1, 1)$ (Spalart *et al.* 1991). The following recursion relation is used to generate a series of polynomials with less computational cost:

$$
\left.
\begin{aligned}
&P_0^{(1,1)}(\eta) = 1, \quad P_1^{(1,1)}(\eta) = 2x \quad \text{and} \\
&4n^2(n+2)P_n^{(1,1)}(\eta) = 2n(2n+1)(2n+2)\eta P_{n-1}^{(1,1)}(\eta) - 2n^2(2n+2)P_{n-2}^{(1,1)}(\eta) \\
&\hspace{9cm} \text{for} \quad n \geqslant 2.
\end{aligned}
\right\} \quad \text{(A 1)}
$$

With a mapping of $\eta \equiv \tanh(y/y_0)$, higher-order Jacobi polynomials are highly oscillatory in the vicinity of the origin and exponentially decaying towards $y \to \pm\infty$ so that they satisfy the homogeneous boundary conditions (2.2).

According to the orthogonality of the Jacobi Polynomials, we normalize them as

$$
\tilde{P}_n(y) \equiv \frac{(1 - \eta(y)^2)P_n^{(1,1)}(\eta(y))}{\sqrt{8y_0(n+1)/(n+2)(2n+3)}}. \quad \text{(A 2)}
$$

The orthogonality can then be simplified as

$$
\int_{-\infty}^{\infty} \tilde{P}_m(\eta(y)) \tilde{P}_n(\eta(y)) \, \mathrm{d}y = \delta_{mn}. \quad \text{(A 3)}
$$

Likewise, the relationship for differentiation can be expressed as

$$
\frac{\mathrm{d}}{\mathrm{d}y}\tilde{P}_0(y) = -\frac{1}{y_0}g(0)g(1)\tilde{P}_n(y) \quad \text{for } n = 0, \quad \text{(A 4\textit{a})}
$$

$$
\frac{\mathrm{d}}{\mathrm{d}y}\tilde{P}_n(y) = -\frac{1}{y_0}g(n)\left[g(n+1)\tilde{P}_{n+1}(y) - g(n-1)\tilde{P}_{n-1}(y)\right] \text{ for } 1 \leqslant n \leqslant N, \quad \text{(A 4\textit{b})}
$$

where

$$
g(n) \equiv \sqrt{\frac{(n+1)(n+2)}{(2n+3)}}. \quad \text{(A 5)}
$$

Thus, the $N \times N$ derivative matrix is generated using (A 4*a*,*b*) neglecting the orders higher than $n > N$, and (2.7) is integrated in $-\infty < y < \infty$ to rewrite it as a matrix equation for the coefficients, c_n. Subsequently, an eigenvalue problem of an $N \times N$ matrix is computationally solved. For a spatial problem, (2.9) is similarly solved.
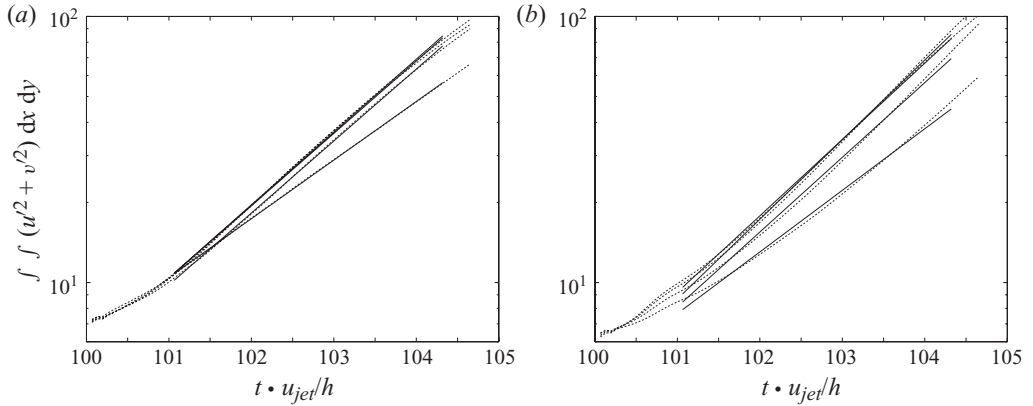
FIGURE 28. Growth of velocity fluctuations initiated with the temporal surrogate eigenfunctions. (*a*) Symmetric mode. (*b*) Asymmetric mode. Wavenumbers are $\alpha = 2.5, 3.0, 2.0$ and 1.5 from the top in both figures. Dotted lines denote the DNS results, and solid lines the fitted slopes.

The accuracy of the spectral method is evaluated based on an analytic velocity profile of $U(y) = 1/\cosh(2y)$ using a larger number of polynomials ($N = 256$) as well as a shooting method applied to an inviscid limit. The error in the most unstable eigenvalue is estimated to be less than 0.01 % in $|\Delta\omega|$ for a temporal problem and 0.1 % in $|\Delta\alpha|$ for a spatial problem. The standard deviation of the corresponding eigenfunctions is within 0.05 % relative to the peak of $|\psi|$ for both problems. Transverse derivatives of eigenfunctions and the mean-velocity profiles are also computed using a spectral method. The accuracy of bi-orthogonal decomposition is then evaluated using symmetric and asymmetric eigenfunctions. The inner product (2.5*b*) between these orthogonal modes is calculated to be less than 0.2 % relative to that of the same modes.

Appendix B. Estimation of temporal growth rates using surrogate eigenfunctions

To construct a two-dimensional eigenfunction for a temporal problem using (2.12), real α must be iteratively calculated until a unique growth rate, i.e. an imaginary part of ω, is found in space. But, in practice the real part of the phase velocity, $\text{Re}[\omega/\alpha]$, is nearly constant in the streamwise extent of our interest. For example, for $\alpha = 2.5$, which is close to the most unstable wavenumber, the real part of ω varies as little as 13 % through $0 \leqslant x/h \leqslant 10$. Therefore, we integrate (2.12) with a constant α to construct a surrogate global eigenfunction for a temporal problem. Such a solution is sufficient to assess the maximum amplification rate of the entire DNS system for this study.

We impose such a surrogate eigenfunction as an initial condition on the top of the mean-velocity field and perform the DNS. By taking the root-mean-square velocity fluctuations inside the patch function, i.e. $(0, 10h) \times (-3h, 3h)$, we can infer the temporal growth rate of the imposed mode (see figure 28). At $Re = 1000$, both symmetric and asymmetric eigenfunctions with several wavenumbers near the most unstable mode ($\alpha = 1.5, 2.0, 2.5$ and 3.0) are examined with the initial magnitude

Case	Re	Grid points ($N_x \times N_y$)	Standard deviations of $\delta u / \delta v / \delta p$ at $(8h, 0)$
B (DNS)	1000	$450 \times 300 / 800 \times 540$	$0.018 u_{jet} / 0.021 u_{jet} / 0.006 \rho u_{jet}^2$
C (DNS)	2000	$600 \times 400 / 1000 \times 640$	$0.016 u_{jet} / 0.022 u_{jet} / 0.008 \rho u_{jet}^2$
C (DNS)	2000	$450 \times 300 / 600 \times 400$	$0.066 u_{jet} / 0.049 u_{jet} / 0.033 \rho u_{jet}^2$
C (Hybrid)	2000	$450 \times 300 / 600 \times 400$	$0.004 u_{jet} / 0.004 u_{jet} / 0.010 \rho u_{jet}^2$
D (Hybrid)	4000	$450 \times 300 / 600 \times 400$	$0.003 u_{jet} / 0.003 u_{jet} / 0.018 \rho u_{jet}^2$
C (DNS/long)	2000	$600 \times 400 / 720 \times 400$ (long)	$0.014 u_{jet} / 0.019 u_{jet} / 0.008 \rho u_{jet}^2$

TABLE 3. Summary of the grid-dependence study and the exit-boundary test. The numbers of grid points compared are listed in the third column, and the standard deviations of streamwise and transverse velocities as well as pressure between them are listed in the fourth column. Statistics are taken during approximately $50h/u_{jet}$ after the first pair of vortices leaves the domain of interest.

of $|u'|_{max} \lesssim 0.01 u_{jet}$. By fitting slopes in logarithmic plots, the largest growth rate is found to be $Im[\omega]_{max} \approx 0.31$ and 0.34 for the symmetric and asymmetric modes, respectively, with both $\alpha = 2.5$. This wavenumber is close to the local peak of the hybrid wavenumber spectrum in figure 11(*b*).

Appendix C. Evaluation of the grid resolution and the exit-boundary condition

First, grid resolution sufficient for the original DNS is inspected. At $Re = 1000$ and 2000, two sets of mesh are tested by running the same condition with the same white-noise inflow forcing of approximately 0.5 % velocity fluctuations. The standard deviations in streamwise and transverse velocities as well as pressure at a sample point, $(x/h, y/h) = (8, 0)$, are then evaluated by comparing the two grids at each Reynolds number, and the results are summarized in the first two rows of table 3. The velocity deviations are found to be approximately 2 % and the pressure deviations to be within 1 % for both cases. The grid resolution for the $Re = 500$ case is set to be the same as that for $Re = 1000$; thereby, the resolution test being omitted at $Re = 500$.

To further reduce the grid resolution at $Re = 2000$ for the hybrid simulation, next we run both DNS and hybrid simulation with two different grids, 600×400 and 450×300, and compare the standard deviations at the sample point in the third and fourth rows of table 3. The results not only demonstrate the insensitivity to the grid resolution in the hybrid simulation but also show that the deviations due to this grid reduction in the hybrid simulation are comparable with or smaller than those associated with the grid resolution in the DNS, mentioned above (i.e. the second row). This justifies quantitative analysis using the 450×300 mesh at $Re = 2000$ in the hybrid simulation. Likewise, because certifying the resolution at $Re = 4000$ based on the DNS is computationally demanding, we similarly evaluate the standard deviations only based on the hybrid simulation and find them to be equally small, as listed in the fifth row of table 3. Thus, we analyse all the hybrid velocity fields solved with 450×300 in this study.

In addition, a test run at $Re = 2000$ for the evaluation of the exit-boundary condition is listed in the last row, where the domains of $[0, 30h] \times [-10h, 10h]$ and $[0, 45h] \times [-10h, 10h]$ are compared. The deviations are on the same order of the grid-resolution test for the DNS at $Re = 2000$.

REFERENCES

AHLUWALIA, D. S. & KELLER, J. B. 1977 Exact and asymptotic representations of the sound field in a stratified ocean. In *Wave Propagation and Underwater Acoustics* (ed. J. B. Keller & J. S. Papadakis), vol. 70, pp. 14–85. Springer.

ARNDT, R. E. A., LONG, D. F. & GLAUSER, M. N. 1997 The proper orthogonal decomposition of pressure fluctuations surrounding a turbulent jet. *J. Fluid Mech.* **340**, 1–33.

BARONE, M. F. & LELE, S. K. 2005 Receptivity of the compressible mixing layer. *J. Fluid Mech.* **540**, 301–335.

BEWLEY, T. R. & LIU, S. 1998 Optimal and robust control and estimation of linear paths to transition. *J. Fluid Mech.* **365**, 305–349.

BLUMEN, W. 1971 Jet flow instability of an inviscid compressible fluid. *J. Fluid Mech.* **46**, 737–747.

BRIDGES, T. J. & MORRIS, P. J. 1984 Differential eigenvalue problems in which the parameter appears nonlinearly. *J. Comput. Phys.* **55**, 437–460.

BROWN, G. L. & ROSHKO, A. 1974 On density effects and large structure in turbulent mixing layers. *J. Fluid Mech.* **64**, 775–816.

CITRINITI, J. H. & GEORGE, W. K. 2000 Reconstruction of the global velocity field in the axisymmetric mixing layer utilizing the proper orthogonal decomposition. *J. Fluid Mech.* **418**, 137–166.

DENISSEN, N. A. & WHITE, E. B. 2009 Continuous spectrum analysis of roughness-induced transient growth. *Phys. Fluids* **21**, 114105.

DRAZIN, P. G. & REID, R. H. 1981 *Hydrodynamic Stability*, 2nd edn. Cambridge University Press.

GASTER, M. 1962 A note on the relation between temporally-increasing and spatially-increasing disturbances in hydrodynamic stability. *J. Fluid Mech.* **14**, 222–224.

HERBERT, T. 1997 Parabolized stability equations. *Annu. Rev. Fluid Mech.* **29**, 245–283.

HILL, D. C. 1995 Adjoint systems and their role in the receptivity problem for boundary layers. *J. Fluid Mech.* **292**, 183–204.

HUERRE, P. 1980 The nonlinear stability of a free shear layer in the viscous critical layer regime. *Phil. Trans. R. Soc. Lond.* **293** (1408), 643–672.

HUERRE, P. & MONKEWITZ, P. A. 1990 Local and global stabilities in spatially developing flows. *Annu. Rev. Fluid Mech.* **22**, 473–537.

KAMPANIS, N. A. & EKATERINARIS, J. A. 2006 A staggered grid, high-order accurate method for the incompressible Navier–Stokes equations. *J. Comput. Phys.* **215** (2), 589–613.

KIM, J. & MOIN, P. 1985 Application of a fractional-step method to incompressible Navier–Stokes equations. *J. Comput. Phys.* **59**, 308–323.

MA, X., KARNIADAKIS, G. E., PARK, H. & GHARIB, M. 2003 DPIV-driven flow simulation: a new computational paradigm. *Proc. R. Soc. Lond.* A **459**, 547–565.

MANKBADI, R. R. 1985 On the interaction between fundamental and subharmonic instability waves in a turbulent round jet. *J. Fluid Mech.* **160**, 385–419.

MASLOWE, S. A. 1991 Barotropic instability of the Bickley jet. *J. Fluid Mech.* **229**, 417–426.

MOLLENDORF, J. C. & GEBHART, B. 1973 An experimental and numerical study of the viscous stability of a round laminar vertical jet with and without thermal buoyancy for symmetric and axisymmetric disturbances. *J. Fluid Mech.* **61**, 367–399.

MORRIS, P. J. 1976 The spatial viscous instability of axisymmetric jets. *J. Fluid Mech.* **77**, 511–529.

MORSE, P. M. & FESHBACH, H. 1953 *Methods of Theoretical Physics*. McGraw-Hill.

NISHINO, K., KASAGI, K. & HIRATA, M. 1989 Three-dimensional particle tracking velocimetry based on automated digital image processing. *Trans. ASME: J. Fluids Engng* **111**, 384–391.

NISUGI, K., HAYASE, T. & SHIRAI, A. 2004 Fundamental study of hybrid wind tunnel integrating numerical simulation and experiment in analysis of flow field. *JSME, Int. J. Ser.* B **47** (3), 593–604.

ORSZAG, S. A. 1971 Accurate solution of the Orr–Sommerfeld stability equation. *J. Fluid Mech.* **50**, 689–703.

REYNOLDS, W. C. & HUSSAIN, A. K. M. F. 1972 The mechanics of an organized wave in turbulent shear flow. Part 3. Theoretical models and comparisons with experiments. *J. Fluid Mech.* **54**, 263–288.

ROGERS, M. M. & MOSER, R. D. 1992 The three-dimensional evolution of a plane mixing layer: the Kelvin–Helmholtz rollup. *J. Fluid Mech.* **243**, 183–226.

SALWEN, H. & GROSCH, C. E. 1981 The continuous spectrum of the Orr–Sommerfeld equation. Part 2. Eigenfunction expansions. *J. Fluid Mech.* **104**, 445–465.

SATO, H. 1960 The stability and transition of a two-dimensional jet. *J. Fluid Mech.* **7**, 53–80.

SFEIR, A. A. 1979 Investigation of three-dimensional turbulent rectangular jets. *AIAA J.* **17** (10), 1055–1060.

SIRISUP, S., KARNIADAKIS, G. E., YANG, Y. & ROCKWELL, D. 2004 Wave-structure iteraction: simulation driven by quantitative imaging. *Proc. R. Soc. Lond.* A **460**, 729–755.

SPALART, P. R., MOSER, R. D. & ROGERS, M. M. 1991 Spectral methods for the Navier–Stokes equations with one infinite and two periodic directions. *J. Comput. Phys.* **96**, 297–324.

SUZUKI, T. & COLONIUS, T. 2003 Inverse-imaging method for detection of a vortex in a channel. *AIAA J.* **41** (9), 1743–1751.

SUZUKI, T. & COLONIUS, T. 2006 Instability waves in a subsonic round jet detected using a near-field phased microphone array. *J. Fluid Mech.* **565**, 197–226.

SUZUKI, T., JI, H. & YAMAMOTO, F. 2009a Unsteady PTV velocity field past an airfoil solved with DNS: Part 1. algorithm of hybrid simulation and hybrid velocity field at $Re \approx 10^3$. *Exp. Fluids* **47** (6), 957–976.

SUZUKI, T. & LELE, S. K. 2003a Green's functions for a source in a boundary layer: direct waves, channelled waves and diffracted waves. *J. Fluid Mech.* **477**, 129–173.

SUZUKI, T. & LELE, S. K. 2003b Green's functions for a source in a mixing layer: direct waves, refracted arrival waves and instability waves. *J. Fluid Mech.* **477**, 89–128.

SUZUKI, T., SANSE, A., MIZUSHIMA, T. & YAMAMOTO, F. 2009b Unsteady PTV velocity field past an airfoil solved with DNS. Part 2. Validation and application at Reynolds numbers up to $Re \leqslant 10^4$. *Exp. Fluids* **47** (6), 977–994.

TAM, C. K. W. & MORRIS, P. J. 1985 Tone excited jets.- Part V. A theoretical-model and comparison with experiment. *J. Sound Vib.* **102** (1), 119–151.

THEOFILIS, V. 2000 On the structure of global linear instabilities and their experimental identification. *Aerosp. Sci. Technol.* **4**, 249–262.

THEOFILIS, V. 2003 Advances in global linear instability analysis of nonparallel and three-dimensional flows. *Prog. Aerosp. Sci.* **39**, 249–315.

TUMIN, A. 1996 Receptivity of pipe Poiseuille flow. *J. Fluid Mech.* **315**, 119–137.

TUMIN, A. 2003 Multimode decomposition of spatially growing perturbations in a two-dimensional boundary layer. *Phys. Fluids* **15** (9), 2525–2540.

TUMIN, A. 2007 Three-dimensional spatial normal modes in compressible boundary layers. *J. Fluid Mech.* **586**, 295–322.

WILLIAMSON, C. H. K. 1996 Three-dimensional wake transition. *J. Fluid Mech.* **328**, 345–407.

YAMAGATA, T., HAYASE, T. & HIGUCHI, H. 2008 Effect of feedback data rate in PIV measurement-integrated simulation. *J. Fluid Sci. Technol.* **3** (4), 477–487.

ZAMAN, K. B. M. Q. & HUSSAIN, A. K. M. F. 1980 Vortex pairing in a circular jet under controlled excitation. Part 1. General jet response. *J. Fluid Mech.* **101**, 449–491.